Dynamics of proton, ion, molecule, and crystal lattice in functional molecular assemblies

Journal:	*ChemComm*
Manuscript ID	CC-FEA-03-2021-001586.R1
Article Type:	Feature Article

Dynamics of proton, ion, molecule, and crystal lattice in functional molecular assemblies

Tomoyuki Akutagawa,* Takashi Takeda and Norihisa Hoshino

Dynamic molecular processes, such as short- or long-range proton (H^+) and ion (M^+) motions, and molecular rotations in electrical conducting and magnetic molecular assembly enable to fabricate the electron $− H^+$ (or M^+) coupling system, while crystal lattice dynamics and molecular conformation changes in hydrogen-bonding molecular crystals have been utilised in external stimuli responsible reversible gas-induced gate opening and molecular adsorption/desorption behavior. These dynamics of the polar structural units are responsible for the dielectric measurements. The H^+ dynamics formed the ferroelectrics and H^+ conductors, while the dynamic M^+ motions of Li^+ and Na^+ involve ionic conductors and the coupling to the conduction electrons. In n-type organic semiconductor, the crystal lattices are modulated by replacing M^+ cations, such as Li^+, Na^+, K^+, Rb^+, and Cs^+. The use of a polar rotator or inverison structures suhc as alkyl amide, *m*-fluoroanilinium cation, and bowl-shaped trithiasumanene π-core enable the formation of ferroelectric molecular assembly. The host–guest molecular systems of ESIPT fluorescent chromic molecule showed interesting molecular sensing properties using various bases, where the dynamic transformation of the crystal lattice and the molecular conformational change were coupled to each other.

1. Introduction

In contrast to inorganic materials, low-molecular-weight organic materials are ideally suited for designing purpose-built molecular assemblies and electronic structures. Among the closest-packing structures in solids, the short- and long-range motion of protons (H^+) and ions (M^+), not to mention molecular rotational freedom, can be introduced into molecular assemblies to achieve partially melted, dynamic crystal lattices.[1] A vast array of physical properties can be realised using these dynamic molecular assembly structures. For example, the collective vibrations in periodically arranged atoms or molecules in the crystal lattice have been recognised as phonons with temperature (*T*)-dependent behaviour, which affects the electrical and thermal conductivities of the lattice.[2] In addition, the energy range of H^+ and M^+ dynamics in solids, although distinctly different from the phonon energy, has the potential to influence the physical properties of molecular assemblies (Fig. 1). Herein, we focus on the various types of thermally activated dynamics of H^+, M^+, molecular rotation, lattice transformation, and molecular conformational change reported in the molecular assemblies of low-molecular-weight organic compounds.[1] In general, dynamic processes (disorder) diffuse phonon dispersion and detracts from the impressive electrical

conductivity and superconductivity of single crystals.[3] Nevertheless, these dynamics play an important role in furnishing biological molecular assemblies with excellent functionality, where the H^+-pump, M^+-channel, and molecular motor work simultaneously to achieve energy conversion efficiencies approaching 100%.[4] This study primarily aims to design artificial molecular assemblies with functionalities comparable to those of biological systems. We believe that this study has the potential to revolutionise the field of material chemistry.

Electron dynamics within the crystal lattice directly affect the electrical conductivity, magnetism, and optical properties of molecular crystals.[5] For instance, the effective overlap of partially filled π-molecules of tetrathiafulvalene (TTF) or 7,7,8,8-tetracyano-*p*-quinodimethane (TCNQ) form a partially filled one-dimensional (1D) π-band in the segregated stacked charge-transfer (CT) complex of (TTF)(TCNQ), which confers the complex with metallic electrical conductivity up to a temperature of 53 K and also results in a Peierls transition to compensate for the electronic stabilisation and lattice distortion of the 1D system.[6] The weight of H^+ is 1836 times greater than that of an electron (e^-), which restricts the motional freedom of H^+ during molecular assembly. However, intra- and intermolecular H^+-transfer (PT) have been extensively examined in terms of memory,[7] laser oscillations,[8] and emission materials.[9] In addition, applications involving ferroelectrics and fuel-cells are directly associated with the short- and long-range motional freedom of H^+ in molecular assemblies.[10,11] The

Institute of Multidisciplinary Research for Advanced Materials (IMRAM), Tohoku University, 2-1-1 Katahira, Aoba-ku, Sendai 980-8577, Japan
E-mail: akutagawa@tohoku.ac.jp

chemical control and design of these H^+ dynamics in molecular assemblies are crucial for improving device performance. For example, short-range H^+ dynamics generate a ferroelectric response in the double-well potential energy curve,[10] while long-range H^+ dynamics have been discussed with regard to H^+ conduction via the Grötthuss and Vehicle mechanisms.[12]

The design of dynamic molecular assembly environments is complicated for situations where the number of M^+ ions far exceeds that of H^+ ; however, such situations do facilitate the development of specific physical properties such as ion conduction, supercapacitance, and ion selective channel formation.[13] Biological systems, in particular, typically exhibit large coupled ionic channels, such as $Na^+–K^+$, $Na^+–Ca^{2+}$, whereby the electrical signals transmitted through the membrane regulate activity and gate ionic transport in the system.[14] Small monovalent cations, such as Li^+ (ionic radius, r_i = 0.59 Å), Na^+ (r_i = 0.99 Å), and Ag^+ (r_i = 0.81 Å), sometimes give rise to diffusion dynamics and ionic transport phenomena in molecular assemblies.[15] Moreover, the short-range motional freedom of M^+ ions is essential to generate polarity in inorganic ferroelectrics, which polar structure is classified to atomic displacement type dipole inversion mechanism found in $BaTiO_3$.[16] In contrast, the long-range motional freedom of M^+ ions corresponds to the ionic conduction rather than ferroelectric behaviour. For instance, the control of Li^+ dynamics is vital to current electronic devices.[17] In organic materials, many Li^+ conductors based on polymers have been developed to improve the conductivity and stability of secondary Li^+ batteries.[18] Recently, Na^+ and Mg^{2+} ionic conductors have also attracted attention for increasing cell capacity without using rare-earth metals.[19] Achieving diffusion dynamics with heavy-weight cations such as Rb^+ and Cs^+ is challenging, and normally results in thermally activated fluctuations.

Furthermore, it is difficult for molecules to exhibit diffusion dynamics in molecular assemblies. However, single crystals constructed from spherical molecules such as adamantane (AD) and C_{60} have demonstrated the order–disorder phase transition of the rotational dynamics for each molecule in the crystal lattice,[20] with such crystals have known as rotator-phase or plastic crystals.[21] To clarify the rotation mechanism, the dynamics in these molecular assemblies have been studied by T-dependent X-ray structural analysis, solid-state nuclear magnetic resonance (NMR), dielectric spectra, neutron inelastic scattering, and optical spectra.[21] Simple rotation dynamics have been examined in methyl (–CH_3) groups of hexamethylbenzene crystals.[22] Various dynamics in molecular assemblies permit thermally activated motional freedoms in the case of small volume changes between the dynamic rotation and frozen states. The presence of large-amplitude motional freedom accompanied by a large apparent volume change destroys the crystal lattice, indicating melting or sublimation without dynamic rotation. Nevertheless, orientation disorder is frequently observed in X-ray structural analyses of single crystals, complicating the task of differentiating dynamic and static environments.[23] Therefore, additional measurement techniques are needed to determine the presence of dynamic

behaviour. However, it should be noted that relatively large structural units exhibit dynamic behaviour in the unit cell. For instance, solid-state molecular rotators and host–guest molecular crystals with specific hydrogen-bonding characteristics display large-amplitude dynamics in the crystal lattice.[24,25] Recently, the elastic and plastic deformations of molecular crystals have been examined to understand mechanical responses and intermolecular interactions in single crystals exhibiting subtle orientation changes for each molecule.[26]

In contrast to single crystals, molecular rotations are allowed in the less ordered plastic and liquid crystal phases, where the random rotations of rod-like, disc-shaped, and spherical molecules are thermally activated in the mesophase between the ordered crystal and liquid phases.[21,27] Sufficient intermolecular interactions occur in these mesophases to maintain the molecular arrangement and prevent melting. In plastic crystal phases, isotropic three-dimensional (3D) rotation,[20] uniaxial 1D rotation of n-alkane crystals,[27] and in-plane rotation of disc-shaped π–molecular crystals[28] have been observed across diverse molecular systems. These dynamic molecular rotations cause an interesting order–disorder structural phase transition, which, unfortunately, is almost independent of the physical properties. Calamitic liquid crystal phases show structural diversity across differently oriented states from nematic (N) to smectic (SmA, SmC, SmB, and SmE) phases.[29] Similarly, discotic liquid crystal phases comprising disc-shaped molecules have a variation in the ordering state of each molecule from discotic nematic (N_D) to hexagonal columnar (Col_h) and rectangular columnar (Col_r) phases,[30] with the latter two assemblies obtained during the stacking of each molecule along the 1D column. In liquid crystal phases, rod-like and disc-shaped molecules rotate thermally along the long axis and the normal to the disc-plane of the molecules, respectively, with the rotation axis termed the director.[29] Typical liquid crystalline molecules have long alkyl chain(s), which are completely melted in the liquid crystal phase and rapid transformation between gauche- and trans-conformations occurs at the C−C−C bonds. Therefore, relatively large-amplitude molecular dynamics are permitted in liquid crystal phases, which can be utilised for the design of dynamic environments that can couple with physical properties.
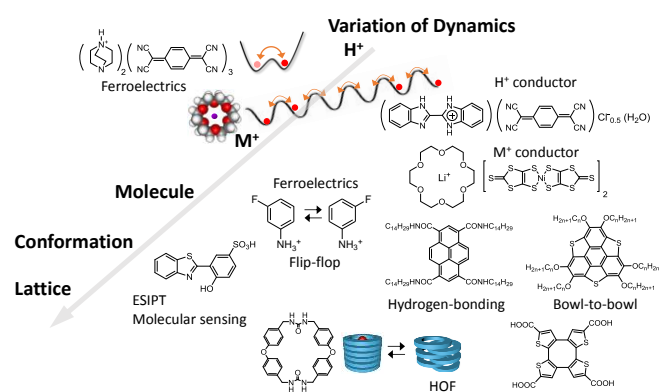
Fig. 1. Variation of dynamics; H⁺, M⁺, molecules, conformation, and crystal lattices in functional molecular assemblies. Molecular structures for fabricating dynamic molecular assembly in this review.

Dynamic transformation of the crystal lattice has been reported in hydrogen-bonded organic frameworks (HOFs),[31] which can exhibit reversible gas and/or molecular adsorption–desorption behaviours. The formation of hydrogen-bonding host−guest molecular crystals has been established in previous studies, making them promising candidates for reversible adsorption–desorption systems for guest molecules.[32] No voids are present in the closest-packing structure of the host lattice, thus minimising the vacuum space for the stabilisation of the lattice energy. However, external stimuli, such as gas or molecular adsorption above the threshold pressure, form a new crystalline space for guest molecules to form hydrogen bonds with the host crystal lattice, indicating the reversible gate opening adsorption–desorption behaviour.[31] This type of dynamic crystal lattice transformation is dominated by multiple intermolecular interactions with different energy scales, including electrostatic, hydrogen-bonding, and van der Waals interactions,[32–34] where the host molecules are bonded by hydrogen-bonding interactions and the guest molecules interact weakly with the host lattice via van der Waals interactions. The latter can be easily modulated by external stimuli associated with the guest adsorption–desorption processes. Therefore, relatively high-energy hydrogen-bonding is utilised to maintain the host crystal lattice, and dynamic structural reconstruction occurs with the aid of weak van der Waals interaction sites during the guest adsorption–desorption cycles. The diversity and anisotropy of the intermolecular interactions in molecular assemblies are fundamental in constructing dynamic hydrogen-bonding crystal lattices, where dynamic crystal lattice transformations sometimes accompany molecular conformational changes and optical responses. Various dynamics in molecular assemblies have been utilised for the design of functional molecular materials (Fig. 1). Although the dynamics of H⁺ and Li⁺ are dominated by small amplitude structural modulation, molecular motion and lattice transformation accompany large magnitude change. Therefore, dynamics in molecular assembly has a scale from H⁺, M⁺, molecule, conformational change, and lattice modulation. Short- and long-range dynamics of small size H⁺ show ferroelectricity and bulk H⁺ conductivity in TCNQ salts. Short- and long-range M⁺ motions in the cavity of crown ethers also appeared the structural phase transition and ionic conductivity, which was coupled with the electronic structure of the π-system. Dynamics of the polar molecule and polar hydrogen-bonding unit have been utilized for an origin of ferroelectricity, while the bowl-to-bowl inversion of non-planar π-system has been also applied for the ferroelectricity. Molecular tautomerism in the excited state is a keto – enol H⁺ dynamics applying for molecular sensing behaviour. Hydrogen-bonding molecular assemblies become a candidate of structurally dynamic system responsible for the outer stimuli. There are variety type of dynamics in molecular assemblies, which can be coupled with physical properties such as H⁺ conduction, M⁺ conduction, ferroelectricity, molecular sensing, molecular sorption

behaviours. Herein, we introduce the representative results of a dynamic molecular system.

2. Evaluations of dynamics

Evaluating molecular assembly dynamics requires several measurement techniques; almost all the dynamic molecular assemblies are observed in the high-T disordered phase after transitioning from the low-T ordered state. The simplest measurement technique is the use of polarised optical microscopy (POM) under the cross-Nicole arrangement, which reveals changes in the birefringence between domains. Each liquid crystal state, such as N, SmA, and SmC, can be characterised based on its texture.[35] In addition, differential scanning calorimetry (DSC) directly determines the phase transition temperature (T_c) and enthalpy change (ΔH); in particular, the first-order phase transition manifests as a sharp phase transition peak, whereas the secondary order phase transition is represented by a notably broader phase transition peak. Significantly, conventional DSC measurements yield the change in transition entropy (ΔS), which is useful for determining the change in the degree of motional freedom due to the phase transition. The magnitude of ΔS is expressed as

$$\Delta S = \Delta H/T = R \ln (W_H/W_L), \qquad (1)$$

where R, W_H, and W_L are the gas constant and the degrees of freedom for the high-T and low-T phases, respectively. When the two orientations are observed at the high-T phase ($W_H = 2$ and $W_L = 1$), ΔS is obtained as $\ln(2) = 5.76$ J K⁻¹ mol⁻¹. For the above case, ΔS is a constant and the ΔH values at $T_c = 10$ and 300 K are 57.6 and 1730 J mol⁻¹, respectively.
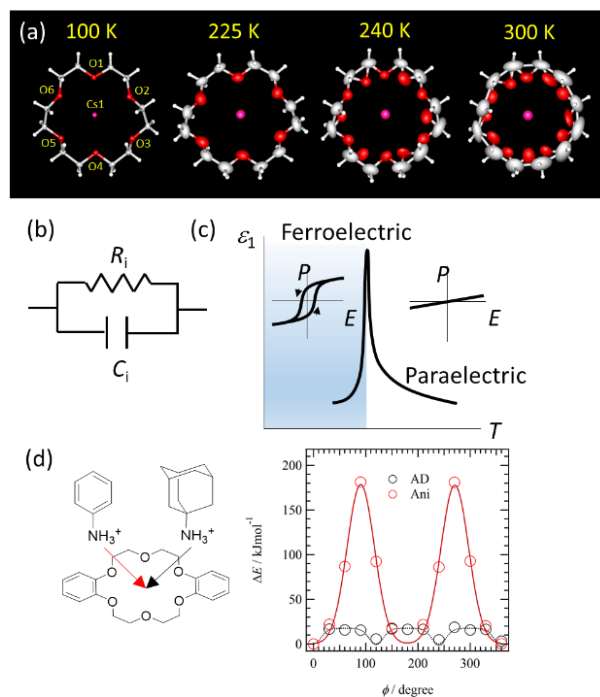
Fig. 2. Techniques for measuring dynamic molecular assembly. (a) T-dependent changes in the orientational disorder from single-crystal X-ray structural analyses. (b) An equivalent electrical circuit for a typical molecular material. (c) Dielectric response and P–E hysteresis curves corresponding to the ferroelectric–paraelectric phase transition. (d) Theoretical calculation of the stepwise rotations for Ani$^+$ and AD-NH$_3^+$ on DB[18]crown-6. A plot of the relative energy change (ΔE, kJ mol^{-1}) and rotation angle (ϕ) for Ani$^+$ (red) and AD-NH$_3^+$ (black) rotators, which have two- and three-fold rotational symmetry, respectively. Figure modified from Ref. 38. Copyright 2005 American Chemical Society.

Other measurement techniques, including T-dependent single-crystal X-ray structural analysis, dielectric spectroscopy, neutron inelastic scattering, optical spectra, solid-state NMR, and theoretical calculations are useful for assessing dynamic behaviour in molecular assembly.[36] In particular, T-dependent solid-state NMR spectroscopy is a powerful measurement tool for observing the local dynamic environment by using a different probe for each nuclear spin.[37] For instance, selectively deuterated species in molecular assemblies can be probed by ^{2}H NMR spectroscopy. Herein, we introduce the key concepts of T-dependent X-ray crystal structural analyses, dielectric spectroscopy, and theoretical calculations in relation to the evaluation of dynamic molecular assemblies.

2.1. Single-crystal X-ray structural analysis

T-dependent powder X-ray diffraction (PXRD) is the standard technique used to identify plastic crystal and liquid crystal phases. Long-range lattice periodicity is indicated by sharp Bragg diffraction peaks, while a broad hallow is typically observed for amorphous or liquid phases, which have a short-range correlation length. In the liquid crystalline Sm phase, sharp diffraction peaks are observed in the low-angle region below $2\theta \sim 10°$ for the layered periodicity, and the complete melting state of alkyl chains is confirmed by the appearance of a broad diffraction peak around $2\theta \sim 20°$.[29] No in-plane periodicity is observed for the SmA and SmC phases, which do not exhibit sharp diffraction peaks around $2\theta \sim 20°$. Symmetry lowering during the transition from the crystal to plastic crystal phase decreases the number of sharp Bragg diffraction peaks drastically. Therefore, T-dependent PXRD measurements provide important insights into the phase transition behaviour from the ordered phase to the dynamic disordered phase.[21]

Single-crystal X-ray structural analysis is applied to determine the molecular and packing structures, where orientational disorder is sometimes observed in the overlap of multiple orientations, leading to the sum of each occupation factor becoming unity. Usually, differentiating static and dynamic orientational disorder is difficult; however, in certain cases, dynamic behaviour can be identified from T-dependent structural analyses. For instance, when the space group and lattice parameter are almost independent of the T-change, observing the second new orientation in the high-T structural analyses implies the transformation from static to dynamic molecular assembly. T-dependent single-crystal X-ray structural analyses of Cs$^+_2$([18]crown-6)[Ni(dmit)$_2$]$_2$ crystals have shown the same space group (P-1) and consistent lattice parameters at 100–350 K.[38] In addition, the non-disordered [18]crown-6 structure was observed at 100 K, while the second disordered orientation emerged at $T \sim 240$ K (Fig. 2a). These two [18]crown-6 orientations overlapped each other at $T > 240$ K, for which the occupation factor was approximately 0.5:0.5.

In addition, the anisotropic thermal ellipsoid of oxygen and carbon atoms was larger in the crystal structures at high-T than at low-T, suggesting the thermally activated six-fold in-plane rotation of the disc-shaped [18]crown-6 molecules in single crystals. These results were consistent with the T-dependent solid-state ^{1}H NMR and ^{133}Cs NMR spectra.[38] When the in-plane rotation symmetry was three-fold, the two orientations overlapped each other and the dynamics were difficult to distinguish via T-dependent X-ray structural analysis.

2.2. Dielectric measurements

The electric circuit of dielectric materials is consistent with a parallel circuit including the intrinsic resistance (R_s) and capacitance (C_s), together with the parasitic reactance and the parasitic resistance of the measurement cable (Fig. 2b).[39] The latter two components can be removed by the guard measurement technique by using a biaxial cable at a measurement frequency (f) below 10 MHz. Samples with a small R_s value correspond to electrical conductors, while those with a large R_s value become insulators or dielectrics. In fact, both components contribute to the solid state electrical property; therefore, the R_s and C_s components are separately measured using AC impedance spectroscopy for both the T- and f-sweeping modes. Typically, a T-range from 4~400 K and a f-range from 100 Hz~1 MHz are utilised in the four-probe method, where the real and imaginary parts of the dielectric constants ε_1 and ε_2 are represented as

$$\varepsilon_1 = (s/r)[B / (2\pi\varepsilon_0 f)] \tag{2}$$

and

$$\varepsilon_2 = (G - \sigma_{DC}) / f, \tag{3}$$

respectively. Here, G and B are the conductance and susceptance, respectively, while s, r, ε_0, and σ_{DC} denote the measurement area, the distance of the electrodes on sample, the dielectric constant in a vacuum, and the DC electrical conductivity, respectively.[39] The dielectric constant is composed of three independent polarisations representing electrons, ions, and the orientation, while the orientational freedom of the dipole moment can be monitored by AC impedance spectra from f = 100 Hz–10 MHz. However, dielectric spectroscopy is less effective for investigating dynamics that do not involve a change in dipole moments.

Ferroelectrics show a sharp dielectric peak at T_c, which indicates the transition from a low-T ferroelectric to a high-T paraelectric phase (Fig. 2c).[40] The T_c value is independent of the measured f value, while the peak intensity depends on the f value. Typical order–disorder organic ferroelectrics are associated with dielectric peaks at low-f conditions around 100 Hz–10 kHz.[41] Ferroelectrics are characterised by typical hysteresis behaviour in the polarisation–electric field (P–E) curve, and the lowering of crystal symmetry at the ferroelectric phase reactivates second harmonic generation (SHG) and the pyroelectric current.[40] However, the contribution of the R_s component increases the leak current and results in an unclear P–E hysteresis curve, which can be improved by a new P–E

measurement method involving a double-wave Positive Up Negative Down (PUND) measurement.[42]

Thermally activated dipole fluctuations without ferroelectric ordering have been observed in T- and f-dependent dipole relaxation process,[39] where the f-dependent ε_1 and ε_2 responses indicate a step-like drop and a peak, respectively. Plotting T- and f-values for each ε_2 peak yields a linear relationship in accordance with Arrhenius-type thermally activated behaviour with an activation energy (E_a). The $\varepsilon_1-\varepsilon_2$ plots (also known as Cole–Cole plots) show a semi-circular profile, and the relaxation time (τ) is obtained from the top f value of the semicircle. For ionic conductors, the ionic conductivity (σ_i) can be determined by the cross-sectional point of the horizontal ε_1 axis.[43] Single-crystal measurements can be useful for evaluating anisotropic dielectric constants, depending on the dimensionality of the dynamics of the polar structural unit. For instance, H^+ dynamics along the 1D hydrogen-bonding chain were observed along the hydrogen-bonding direction, while there was no response along the measurement normal to the 1D chain. Therefore, the dielectric measurement using pellet sample unclarified the dielectric peak. Elucidating the dielectric anisotropy allows the mechanism of the molecular assembly dynamics to be discussed.

2.3. Theoretical calculations

Intra- and intermolecular H^+-transfer in the hydrogen-bonding network and molecular rotation in single crystals have been discussed with reference to theoretical calculations of the potential energy curve along the motional coordinates. When the atomic coordinates are obtained via single-crystal X-ray structural analysis, the dynamic units, such as H^+, or molecules are virtually moved to calculate the total energy for each atomic coordinate. For instance, the potential energy curves for the molecular rotations of anilinium (Ani^+) and adamantylammonium ($AD-NH_3^+$) ions on [18]crown-6 have been obtained through the virtual rotations of Ani^+ and $AD-NH_3^+$, thereby clarifying the two- and three-fold rotational symmetry of Ani^+ and $AD-NH_3^+$, respectively, according to the molecular structures of the rotators.[44] Isolated rotator – stator structure usually shows free rotation with small magnitude of rotation barrier around several kJ mol^{-1}. However, the rotation energy is closely affected by the nearest-neighbouring unit in the closet-packing structure, which shows steric hindrance for the rotations. Although rotational symmetry was reproduced in the calculation, the magnitude of the potential energy barrier (ΔE) was inconsistent with the experimental value. In the present calculation, only the nearest-neighbouring units were considerably included in the calculations. However, the collective motion of crystal lattice plays an important role to deform and relax the steric hindrance for the molecular rotation, which decreased an actual rotation barrier. The thermal energy at 300 K ($k_B T \sim 2.3$ kJ mol^{-1}) was considerably smaller than the calculated ΔE value.[44] However, actual molecular rotations were observed in the dielectric and solid-state NMR measurements for a relatively large ΔE of approximately 100 kJ mol^{-1},[45] where the collective lattice distortion effectively decreased the ΔE value.

A simple hydrogen-bonding system has been discussed in the double-well potential energy curve for the H^+ coordinate. When the sum of $k_B T$ and the applied outer energy (E_{out}) is larger than ΔE, PT and dipole inversion occur in the hydrogen-bonding network. Homo-type hydrogen-bonding systems, such as $O-H\cdots O$ and $N-H\cdots N$, which possess the same heteroatoms, form a symmetrical double-well potential energy curve for the PT process, while the hetero-type systems, such as $N-H\cdots O$ and $O-H\cdots N$, which possess two different heteroatoms produce an asymmetrical double-well potential energy curve and tend to exhibit H^+ localising on one side of the heteroatom.[46] In general, the PT process occurs readily in homo-type hydrogen-bonding networks. In addition, the magnitude of the potential energy barrier, ΔE, is an important parameter governing proton-transfer, where strong hydrogen-bonding interactions with short $X\cdots X$ distances (d_{X-X}) decrease the magnitude of ΔE. A relatively strong hydrogen-bonding interaction was observed at $d_{O-O} < 2.5$ Å in the $O-H\cdots O$ hydrogen-bonding structure, which shows a single minimum potential energy curve in the absence of intermolecular proton-transfer. In the single minimum potential energy curve, the order-disorder phase transition of the protonic orientation should be completely suppressed. The quantum paraelectric state, arising due to the quantum protonic frustration, was observed in the low temperature phase in the absence of the protonic ordering ground state. Lowering in the ΔE of the double-wall potential energy curve is favorable for intermolecular proton transfer and order-disorder phase transition at relatively low temperatures. In the ferroelectric phase, the coercive electric field (E_{th}) is also decreased by low ΔE caused by lowering the dipole inversion energy, whereas the elongation of the intermolecular hydrogen-bonding distance increases the dipole moment, μ, and remanent polarization (P_r).

3. Dynamics of H^+

In contrast to e^- dynamics, molecular assemblies are rarely designed to promote H^+ dynamics. Hydrogen can exit at three different form of hydride (H^-), hydrogen atom ($H^\bullet$), and proton (H^+), which transfer and storage are important technologies in the environmental friendly energy consumption. Hydride (H^-) ions are an interesting hydrogen species, with H^--transfer playing an important role in chemical reactions in biological systems such as nicotinamide adenine dinucleotide (NADH).[47] Incorporating functional molecular assembly with the H^--transfer process is a major objective in the design of physical properties. Although our next target is chemical control of dynamic behaviour of H^- species in molecular assembly, there is no ideal for controlling in the dynamics of H^- to associate with physical property. Herein, we focus predominantly on short- and long-range PT systems as well as H^+-e^- coupling phenomena in electrically conducting molecular assemblies.

3.1. Short-range H^+ motion

The H^+ dynamics in the $X-H\cdots Y(X)$ hydrogen-bonding network show thermally activated fluctuation states between

X−H$^+$•••Y(X) and X•••H$^+$−Y(X) structures, whose motion is dictated by the double-minimum potential energy curve for the H$^+$ coordinate.[46] Simply, intermolecular PT can be controlled via the acidity (pK_a) of the H$^+$ donor (HD) and the acidity of the conjugated acid of the H$^+$ acceptor (HA$^+$).[48] In the X−H$^+$•••Y(X) system, pK_a value differences, $\Delta pK_a = pK_a(HD) - pK_a(HA^+)$, are a useful indicator of the PT state in molecular assemblies. When ΔpK_a approaches zero, a strong hydrogen-bonding interaction with a small ΔE is observed.[49] Strong hydrogen-bonding interactions decrease the ΔE value, resulting in a single-minimum (rather than double-minimum) potential energy curve. For example, a single-minimum potential energy curve has been observed in strong O•••H•••O hydrogen-bonding interactions with an O•••O distance less than 2.4 Å; in such cases, the H$^+$ exists at the midpoint between the two O atoms.[34,49,50] The intramolecular hydrogen-bonding system has a tendency to form relatively strong interactions. For instance, quantum H$^+$ tunnelling in strong zero-dimensional O•••H•••O hydrogen-bonding interactions has been reported in 5-bromo-9-hydroxyphenalenon and ferroelectric K$^+$H$_2$PO$_4^-$ (KDP) crystals.[51,52] Furthermore, keto (=O) and enol (−OH) tautomerism shows an interesting structural and electronic transformation, and the excited-sate intramolecular proton transfer (ESIPT) indicates fluorescence owing to a large Stokes shift exceeding 10,000 cm^{-1}, which makes such tautomers suitable for use as near-infrared fluorescent probes for biological sensing.[53,54]
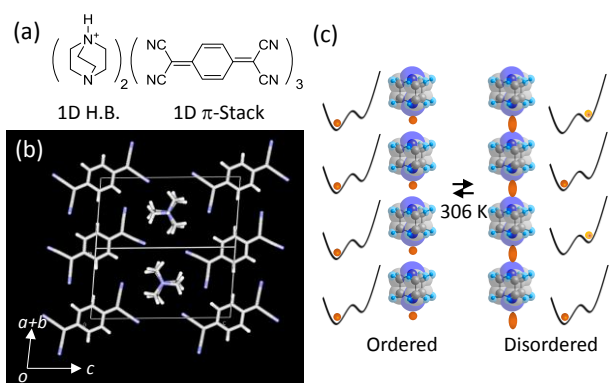

Fig. 3. *T*-dependent order−disorder phase transition of PT in the 1D N−H$^+$•••N hydrogen-bonding chain. (a) Molecular structure of (HDABCO$^+$)$_2$(TCNQ)$_3$. (b) Unit cell viewed along the 1D (N-H$^+$•••N)$_\infty$ hydrogen-bonding chain and electrical conducting π-column of TCNQ. (c) The ordered state of H$^+$ generates a macroscale dipole moment along the 1D chain, while the thermal fluctuation of H$^+$ in the double-minimum potential energy curve delocalises each H$^+$ in the N•••H$^+$•••N hydrogen-bonding system.

The motional freedom of H$^+$ in the hydrogen-bonding system is followed by an ice rule without the formation of disproportional H$^+$ species;[34] instead, a collective PT process occurs along the hydrogen-bonding chain. For instance, the collective PT in the 2D O−H•••O hydrogen-bonding network of squaric acid (SQ) single crystals accompanies the structural reconstruction between the C−C and C=C (O−H and =O) bonds of the SQ molecule. This indicates that a paraelectric–antiferroelectric phase transition occurs at 375 K.[55] In the high-*T* paraelectric phase, the melting state of the H$^+$ lattice in the O•••H•••O network generates thermally fluctuating H$^+$ ions in the 2D layer. Interestingly, the ferroelectric ordering of croconic acid crystals has been observed as a slight structural anomaly in SQ molecules.[56] The PT processes accompanying changes in the dipole moment can be detected using dielectric measurements.

The 1D N−H$^+$•••N hydrogen-bonding chain of mono-protonated 1,4-diazabicyclo[2.2.2]octane (HDABCO$^+$) generates a macroscale dipole moment, for which the appearance of PT with the melting state of the H$^+$ lattice is determined by the magnitude of $k_BT + E_{out}$ rather than ΔE. When all hydrogen-bonding dipole structures are inverted in response to applying E_{out}, a ferroelectric ground state is observed in the molecular assembly. Indeed, ferroelectric–paraelectric phase transitions have been reported in simple salts of (HDABCO$^+$)(BF$_4^-$) and (HDABCO$^+$)(ClO$_4^-$).[57] We introduced this ferroelectric hydrogen-bonding 1D N−H$^+$•••N chain into the semiconducting TCNQ salt (Fig. 3a), forming (HDABCO$^+$)$_2$(TCNQ)$_3$, an electrically conducting anion radical salt.[58] The π-stacking column of TCNQ and the N−H$^+$•••N hydrogen-bonding chain were aligned parallel to each other (Fig. 3b), where the dielectric constant along the hydrogen-bonding chain showed a dielectric peak at 306 K for low-*f* measurements (i.e., < 10 kHz). The dielectric peak disappeared along the normal to the 1D hydrogen-bonding chain. In addition, the deuterated effect of the N−D$^+$•••N hydrogen-bonding chain raised its T_c to 376 K, suggesting the presence of H$^+$ dynamics in the hydrogen-bonding chain. Single-crystal X-ray structural analysis at 100 K revealed H$^+$ localisation at a single N-site in the N−H$^+$•••N interaction, while at 350 K, the electron density was found to coincide with the midpoint between the two N-sites in the N•••H$^+$•••N structure (Fig. 3c). These H$^+$ dynamics are dominated by the double-minimum potential energy curve for H$^+$ coordinates, where the localisation–delocalisation of the H$^+$ position is directly associated with the order–disorder phase transition of the ferroelectrics. By applying an $E_{out} + k_BT$ that exceeds ΔE, the direction of the dipole moment between the N−H$^+$•••N and N•••H$^+$−N orientations can be inverted. The existence of electrical conductivity in the TCNQ π-stack (10^{-3} S cm^{-1} at 298 K) affected the *P−E* hysteresis curve of the ferroelectric phase. However, the σ_{DC} value of (HDABCO$^+$)$_2$(TCNQ)$_3$ was slightly influenced by the ferroelectric–paraelectric phase transition, suggesting a weak coupling between the ferroelectric polar chains with internal electric field and the conduction electrons on the TCNQ stacks.

3.2. Long-range H$^+$ motion

Long-range H$^+$ dynamics have been observed in H$^+$ conduction, which has important implications for fuel-cell applications.[11] Nevertheless, maximising the proton conductivity (σ_{H+}, S cm^{-1}) in molecular assemblies remains an ongoing challenge. The conductivity of solids is expressed as follows:

$$\sigma = ne\mu, \qquad (4)$$

where n, e, and μ are the carrier density, charge, and mobility, respectively. The chemical design of n and μ determines the magnitude of σ_{H+}. For e$^-$ transport, both n and μ are controlled

Journal Name ARTICLE

according to the chemical design of the molecular arrangement and/or physical devices such as field effect transistors (FETs),[59] where herringbone and brick-like stacking arrangements of 2D electrical conducting layers have been utilised to increase the μ value. Conversely, there is no useful design strategy for increasing the σ_{H+} value controlling n and μ during molecular assembly. Additionally, no chemical means of controlling the strength of hydrogen-bonding interactions have been established. Strong, uniform, high-dimensional hydrogen-bonding networks are considered an effective approach for increasing the magnitude of μ. Controlling the n value relies on the coexistence of many H^+ carriers in the molecular assembly. Chemical control of hydrogen-bonding interactions can effectively increase the σ_{H+} value, which should be correlated with the crystal structures. However, anisotropy measurements of σ_{H+} using single crystals have been used to identify a correlation between the hydrogen-bonding pattern and the magnitude of σ_{H+} in various molecular assemblies.

A use of $H_2PO_4^-$ unit is one of the useful method to increase the σ_{H+} value. For instance, a high σ_{H+} value of 2.2×10^{-2} S cm^{-1} at 513 K has been reported in the inorganic salt CsH$_2$PO$_4$,[60] where the uniform intermolecular O−H•••O hydrogen-bonding network between $H_2PO_4^-$ anions and the rotation of spherical $H_2PO_4^-$ anions increase the σ_{H+} value. In contrast, replacing Cs$^+$ cations with K$^+$ cations formed to the ferroelectric crystal KDP (with T_c = 122 K).[52] In this case, the chemical design of the cation in the $H_2PO_4^-$ anion is essential in enabling long- and short-range H^+ dynamics. Herein, we focused on the single crystals of $H_2PO_4^-$ salts with various organic cations, which were tuned by replacing the original cations with conventionally available organic cations. Among them, the O−H•••O hydrogen-bonding networks of $H_2PO_4^-$ anions with Ani$^+$ and 2,2'-diaminobithiazolium (2,4-H2DABT^{2+}) cations formed a variety of hydrogen-bonding patterns and σ_{H+} values, and the anisotropic σ_{H+} values in single crystals were evaluated precisely.[61,62] The trivalent H^+ source of H$_3$PO$_4$ can generate $H_2PO_4^-$ anion and HPO$_4^{2-}$ dianion species, both of which can form O−H•••O hydrogen-bonding networks in molecular assemblies. From the organic cation variations, we selected the conventional Ani$^+$ derivative bearing halo substituents of F, Cl, Br, and I at the o-, m-, and p-positions, which were easily introduced into the $H_2PO_4^-$ salts. In contrast, the π-planar DABT molecule has two di-protonated structural isomers, namely 2,4-H2DABT^{2+} and 2,5-H2DABT^{2+}, which have almost identical molecular structures (Fig. 4a).[62] However, these two isomers can generate different crystal structures and σ_{H+} values in the 2D or 3D H^+ conducting layers. Eighteen distinct single crystals were obtained by combining either Ani$^+$ or DABT and H$_3$PO$_4$ in solution phase, which clarified the correlation between hydrogen-bonding patterns and σ_{H+} value magnitudes. First, we confirmed that divalent HPO$_4^{2-}$ salts do not exhibit σ_{H+} behaviour, while H2DABT^{2+} salts exhibit an interesting mixed proton state, ($H_2PO_4^-$)(H$_3$PO$_4$), in response to changing the crystal growth conditions. These mixed protonated crystals included multiple H^+ carriers and increased n values.

Figure 4b summarises the schematic representations of five varieties of hydrogen-bonding network based on 2,4-H2DABT^{2+} and 2,5-H2DABT^{2+} salts with $H_2PO_4^-$ anions, where single and double O−H•••O hydrogen-bonding interactions are observed between adjacent $H_2PO_4^-$ anions.[62] The typical O−H•••O 1D chain structure was elongated in type-I salts, where single and double hydrogen-bonding interactions alternated along the chain direction. On the contrary, 2D O−H•••O networks were observed in type-II and type-III salts, although only the single O−H•••O hydrogen-bonding interaction was observed in the type-II salts. Type-IV and type-V salts both formed 3D O−H•••O networks, with the hydrogen-bonding interactions in type-V salts showing greater uniformity than in the type-IV salts. Notably, O−H•••O hydrogen-bonding networks with high uniformity and dimensionality demonstrated considerably higher σ_{H+} values. The hydrogen-bonding networks of these molecular crystals are rather complicated and involve a complex H^+ conduction mechanism. However, anisotropic σ_{H+} measurements of single crystals clarified the relationship between the hydrogen-bonding pattern and the σ_{H+} value, which is vital for designing high σ_{H+} materials. Recall that uniform and strong hydrogen-bonding interaction tend to show much higher σ_{H+} values.
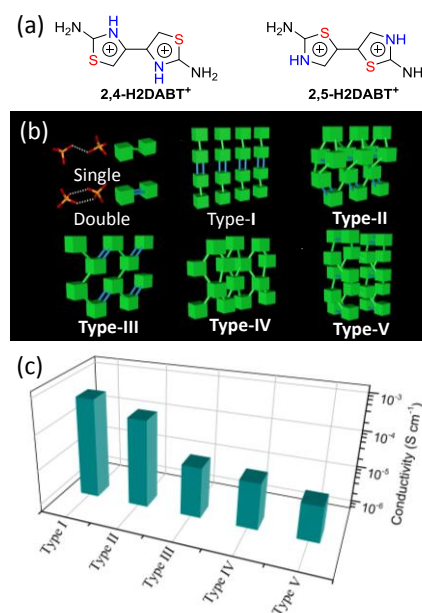

Fig. 4. (a) Structures of H^+ conducting $H_2PO_4^-$ salts with structural isomers of 2,4-H2DABT^{2+} and 2,5-H2DABT^{2+}. (b) Schematic of type-I, -II, -II, -IV, and -V hydrogen-bonding structures. Single and double O−H•••O hydrogen-bonding interactions between $H_2PO_4^-$ anions are drawn in green and blue lines, respectively. (c) Maximum σ_{H+} values for each hydrogen-bonding type. Figure modified from Ref. 62. Copyright 2020 American Chemical Society.

Controlling the n value for H^+ conduction during molecular assembly is a difficult task, particularly considering that the H^+ carrier of $H_2PO_4^-$ anions can exist on any of the four O sites of the anion in a highly localised environment. Unfortunately, the doping procedure and control of the H^+ carrier concentration have not been established. When the different protonated states were obtained at ($H_2PO_4^-$)$_{0.5}$(H$_3$PO$_4$)$_{0.5}$, $H_2PO_4^-$, and HPO$_4^{2-}$, the n value for these three states decreases, yielding values of

2.5, 2, and 1, respectively, suggesting that the $(H_2PO_4^-)_{0.5}(H_3PO_4)_{0.5}$ mixed protonated state is a good candidate for generating multiple H^+ carriers and increasing n. However, an efficient method for designing such mixed H^+ states to control the n value in H^+ conducting organic materials has yet to be established.

3.3. $H^+ - e^-$ coupling

The dynamic $N-H^+\bullet\bullet\bullet N$ hydrogen-bonding chain in $(HDABCO^+)_2(TCNQ)_3$ showed a paraelectric–ferroelectric phase transition, where the H^+ dynamics were weakly coupled with the conduction electrons on the TCNQ column.[58] Simultaneous dynamics involving H^+ ions and CT interactions between aniline and nitrophenol derivatives have been reported in binary molecular complexes by Saito and Matsunaga,[63] where the ionic ground state of $(Ani^+)(nitorophenolate^-)$ salts transformed to the neutral (aniline) (nitrophenol) complex in response to increasing T. The apparent colour change of crystals from yellow to red-green through CT interactions was observed in the high-T phase; other physical properties were not affected by the phase transition. Quinhydrone crystals are well-known hydrogen-bonding CT complexes, with properties between weak electron donors of hydroquinone (H2Q) and weak electron acceptors of p-benzoquinone (BQ).[64] The role of the semiquinone neutral radical state (HQ$^\bullet$) in the generation of a new electronic phase of degenerate neutral radical species in crystals has been discussed by Mitani and Saito.[65] Unfortunately, such HQ$^\bullet$ states have yet to be obtained under ambient conditions, with pressures as high as 30 kbar required to generate the HQ$^\bullet$ species in solids. Moreover, the physical properties of HQ$^\bullet$ crystals, such as electrical conductivity and magnetic susceptibility, have not been examined. Recently, cation radical salts of hydrogen-bonding catechol-fused TTF molecules have been reported to exhibit an interesting electrical conducting property when coupled with the PT in $O-H\bullet\bullet\bullet O$ hydrogen-bonding interactions, with the deuterated effect observed in the electrical conducting behaviour.[66] The H^+ dynamics play an important role in the electrical conductivity of the π-stack of TTF, suggesting relatively strong H^+-e^- coupling phenomena in the electrically conducting crystals.

Fig. 5. Schematic of the H^+-e^- coupling system of H2BBIM in TCNQ. (a) Multiple H^+ and e^- transfer diagram of 2,2'-bi-1H-dibenzoimidazole (H2BBIM). (b) Uniform π-stacking structure of TCNQ and H3BBIM$^+$ in (H3BBIM$^+$)(TCNQ)(Cl$^-$)$_{0.5}$(H$_2$O) single crystals. (c) 1D hydrogen-bonding channel between the π-stacking columns of H3BBIM$^+$, where Cl$^-$ anions (yellow) and H$_2$O molecules (red) occupy the channel in addition to highly acidic H^+ ions.

Using the concept of H2Q−BQ coupling, we focused on multiple H^+ and e^- transfer systems based on 2,2'-bi-1H-imidazole (H2BIM), which has a complicated $4H^+-4e^-$ system, to design strong H^+-e^- coupling in a crystalline state (Fig. 5a).[67] In the 2,2'-bi-1H-benzeimidazole (H2BBIM) molecule, the fully oxidised BBIM was isolated as a $5\pi-5\pi$ electron acceptor, while the $7\pi-7\pi$ electron donor of H4BBIM was difficult to identify. However, all closed-shell H^+ species, including H4BBIM^{2+}, H3BBIM$^+$, H2BBIM, HBBIM$^-$, and BBIM^{2-}, were isolated as the stable $6\pi-6\pi$ electron system, and were introduced into the counter cation or anion in electrically conducting radical salts.[68] The electrochemical reduction of TCNQ in the presence of (H3BBIM$^+$)Cl$^-$ formed black single crystals of (H3BBIM$^+$)(TCNQ)(Cl$^-$)$_{0.5}$(H$_2$O), which showed a high electrical conductivity of 10 S cm^{-1} at 298 K.[68] Structural analysis of the crystals revealed segregated uniform π-stacks of H3BBIM$^+$ and partially reduced TCNQ$^{-0.5}$ (Fig. 5b). Additionally, the 1D hydrogen-bonding channel was elongated between the H3BBIM$^+$ columns. The channel was occupied by Cl$^-$ anions and H$_2$O molecules, as well as highly acidic H^+ arising from the H3BBIM$^+$ cation (Fig. 5c). T-dependent σ_{H+} values were measured using the H^+ blocking electrode of Nafion films, which indicated an σ_{H+} value of 10^{-3} S cm^{-1} at 298 K. In the high-T region, both the H^+ ions and the H_2O molecules thermally fluctuate and melt in the channel, while these dynamics freeze when the T is lowered, and the electrical conductivity and magnetic susceptibility are modulated by H^+ dynamics. The H^+ localisation in the 1D channel affects the conduction electrons on the TCNQ stack via the generation of the charged pinning potential. A similar order–disorder phase transition involving the coupling of H^+ dynamics with the conduction electrons on the TCNQ stack has been observed by Kitagawa et al. in the Pd-coordination complex of diaminoglyoxim with TCNQ.[69]
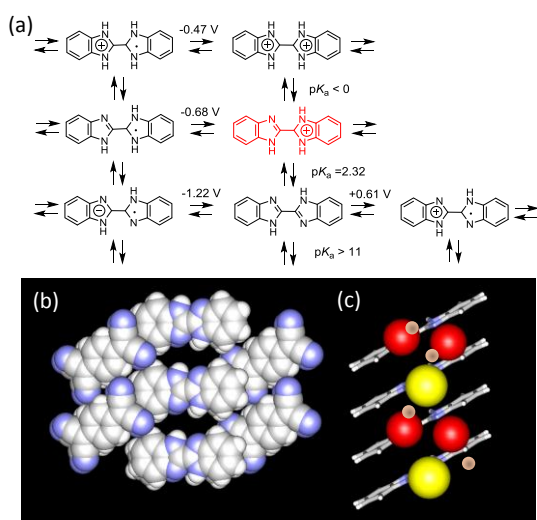
4. Dynamics of ions

Short-range ionic displacement in inorganic ferroelectrics such as $BaTiO_3$ indicates a bistable dipole arrangement, while long-range ionic motion has been observed in ion-conducting perovskites, including vacant oxygen sites.[70] Previously, M^+ dynamics in closed-packing molecular crystals have been chemically designed using a supramolecular approach,[71] often involving small Li^+ and Na^+ ions.

4.1. Short-range M^+ motion

Crown ethers can selectively encapsulate M^+ ions within the molecular cavities, thereby forming M^+/crown-ether supramolecular cations.[72] As opposed to simple inorganic anions, various functional counter anions are utilised as supramolecular cations to design functional molecular

crystals.[73] The central pore of crown ether forms dynamic M^+ environment in single crystals (Scheme 1). Small size $M^+ = Li+$ and Na^+ in contrast with cavity of [18]crown-6 allows the motional freedom to exist M^+ at the upper and the lower position to the molecular plane of [18]crown-6. On the contrary, regular array of [18] crown-6 formed the ionic channel for small size Li^+ and Na^+, where the M^+ can flow along the 1D channel by the application of the outer electric filed. In biological channel, M^+ selectivity, gated, and passive M^+ transport have been observed. Such artificial M^+ channel is one of essential structural unit for the feature molecular machines. Herein, we utilised electrically conducting or magnetic TCNQ and $[Ni(dmit)_2]$ anions to realise M^+/crown-ether supramolecular cation combinations (Fig. 6a). Short-range Li^+ and Na^+ dynamics were successfully designed to form [15]crown-5 and [18]crown-6 for the semiconducting TCNQ salts.[74] The size mismatch between M^+ ions and pores of crown ethers is important for generating a dynamic environment in single crystals.
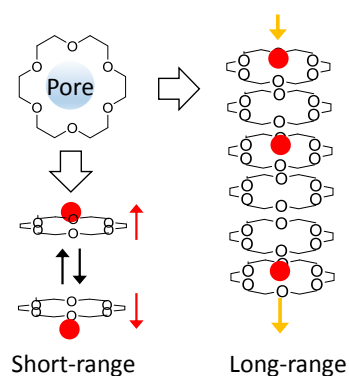
Scheme 1. Fabrication of dynamic environment using central pore of [18]crown-6. Isolated M^+([18]crown-6) structure with the upper and lower M^+ position to [18]crown-6 plane (left). Regular array of [18]crown-6, forming ionic channel and long-range M^+ motion along the 1D pore.

Semiconducting TCNQ salts comprising all possible combinations of M^+ (Li^+ or Na^+) and crown ethers ([12]crown-4, [15]crown-5, or [18]crown-6) were examined by Sambe et al. Specifically, the authors systematically investigated which crystal structures, dielectric responses, electrical conductivities, and magnetic susceptibilities were optimum for designing dynamic structures.[74] Notably, structural phase transitions coupled with Li^+ and Na^+ dynamics were observed in Li^+([15]crown-5)$(TCNQ)_2$ and Na^+([15]crown-5)$(TCNQ)_2$ (Figs. 6b and 6c). T-dependent single-crystal X-ray structural analyses of Li^+([15]crown-5)$(TCNQ)_2$ at 100 and 200 K clarified the T-dependent Li^+ coordination environment for five O atoms of [15]crown-5 and two –CN groups of the two TCNQ stacks at axial positions, where the asymmetrical axial –CN coordination to Li^+ was observed in the crystal structure at 100 K. After the structural phase transition, the unit cell at 200 K was reduced to half its volume in the low-T phase, where the orientational disorder of [15]crown-5 and the equivalent –CN coordination to Li^+ from the two TCNQ stacks were observed in the high-T crystal phase. These structural changes were consistent with the T-dependent dielectric measurements, and the dynamic Li^+ motion affected both the structural phase

transition and the change in crystal symmetry. The formation of a strong TCNQ π-dimer was observed in the orthogonally interacting packing structure, forming a 2D electrical conducting layer. Such 2D conducting layers have not been observed in previous studies involving TCNQ stacks and show a relatively high electrical conductivity of 1 S cm^{-1} at 298 K despite the non-uniform π-dimer arrangement. A similar structural phase transition, as well as the formation of a 2D layer of TCNQ stacks, was observed in Na^+([15]crown-5)$(TCNQ)_2$.

The crystal structure of Li^+([18]crown-6)$(TCNQ)_2(H_2O)_2$ was constructed by a non-uniform 1D π-dimer stack of TCNQs with an electrical conductivity of 1.8×10^{-3} S cm^{-1} at 298 K. In the crystals, T-dependent Li^+ dynamics were observed inside the Li^+([18]crown-6)$(H_2O)_2$ supramolecular cations. The single-crystal X-ray structural analysis at 100 K indicated the two orientations of the Li^+ cation at the left and right pore boundaries of [18]crown-6, where H_2O molecules interacted with Li^+ at the pentagonal structure representing the $Li^+ \cdots O_5$ coordination environment (Fig. 5d). The dynamics of the Li^+ cations inside [18]crown-6 were observed in both the T- and f-dependent dielectric constants, indicating two Debye-type relaxation peaks corresponding to ε_2 values at 100 and 150 K. The dielectric constants were measured along the direction normal to the TCNQ stack, which removed the contribution from the electrical conductivity. According to the masses of Li^+ and H_2O, these low-T and high-T dielectric relaxations were assigned to the Li^+ and H_2O dynamics, respectively. Unfortunately, the coupling between the Li^+ dynamics and the conduction electrons on the TCNQ stack was too weak to have a meaningful impact. The dynamics of Na^+ ions within polyoxomethalate were successfully coupled with its ferroelectric properties by Nishihara et al., who reported a ferroelectric-like response in the $P–E$ hysteresis curve.[75] The Na^+ displacement inside the cavity of polyoxomethalate induced dipole inversion; however, T-dependent dielectric constants were inconsistent with the typical ferroelectric behaviour associated with simple Debye-type relaxation. Single-molecule ferroelectrics have been proposed in this system.
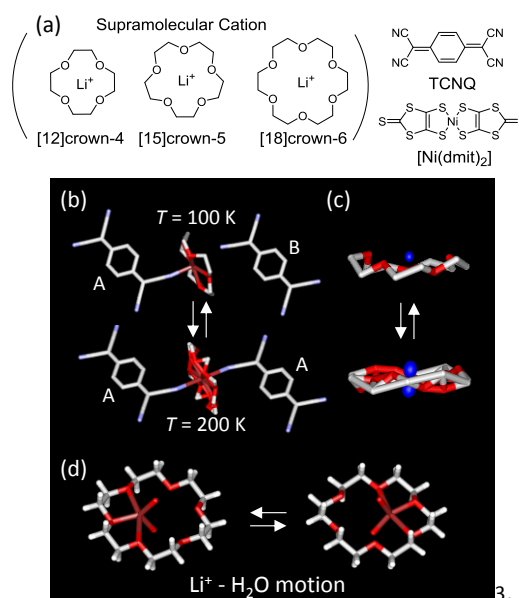

(a) Supramolecular Cation

[12]crown-4   [15]crown-5   [18]crown-6

TCNQ

$[Ni(dmit)_2]$

(b) T = 100 K
T = 200 K
(c)
(d) Li^+ - H_2O motion

Fig. 6. Dynamic M^+ cations inside the cavity of crown ethers. (a) Dynamic Li^+ cation in [15]crown-5 and [18]crown-6 in TCNQ and $[Ni(dmit)_2]$ salts. (b) Structural phase transition coupled with dynamic Li^+ (or Na^+) cations inside the cavity of [15]crown-5. (c) Side views of Li^+ (or Na^+) positions in the low-T and high-T phases and the orientational disorder of [15]crown-5 in the high-T phase. (d) Li^+ and H_2O dynamics within the cavity of [18]crown-6. Figure modified from Ref. 74. Copyright 2020 American Chemical Society.

4. 2. Long-range M^+ motion

Long-range M^+ dynamics result in ionic conduction during molecular assembly. Small Li^+ and Na^+ cations can form a 1D ionic channel consisting of a regular array of [15]crown-5 and [18]crown-6 molecules, with thermally activated Li^+ and Na^+ dynamics observed in the electrically conducting $[Ni(dmit)_2]$ salts (Fig. 7a).[76] In the TCNQ salts, ionic channel formation has not been observed for any of the aforementioned combinations of M^+ ions and crown ethers, suggesting the importance of molecular structure of the counter anion.[74,77] Single crystals of $Li^+_x([15]crown-5)[Ni(dmit)_2]_2(H_2O)$ (where x is less than unity) exhibit high electrical conductivity at approximately 100 S cm^{-1} at 298 K, and the presence of Li^+ dynamics was confirmed by solid-state ^7Li NMR spectra.[76a] Using an electron blocking electrode comprising Li^+(polyethyleneoxide)X^- to evaluate Li^+ conductivity (σ_{Li+}) revealed a σ_{Li+} value of 10^{-6} S cm^{-1} at 298 K, which was eight orders of the magnitude lower than the electrical conductivity. The Li^+ dynamics in the 1D channel influenced the localisation–delocalisation behaviour of the conduction electrons on the $[Ni(dmit)_2]$ stacks. Lowering the T decreased the thermally activated Li^+ dynamics in the channel, which generated a positively charged pinning potential for the conduction electrons.[76b] In contrast, large Cs^+ cations in the regular array of [18]crown-6 molecules cannot pass through the central cavity of [18]crown-6. However, a relatively high electrical conductivity was observed for $Cs^+_x([18]crown-6)[Ni(dmit)_2]_2$ crystals even at 10 K, which was attributed to the regular arrangement and high polarisability of Cs^+ cations in the channel.[76b]

The crystal lattice of these ionic salts is governed primarily by the electrostatic cation–anion Coulomb interaction, which shows high thermal and chemical stability even in organic materials. For instance, the benzenesulfonate (BS^-)-substituted bis(naphthalene diimide) (NDI), π-molecular framework has excellent n-type semiconducting properties, with the Na^+ salt of $(Na^+)_2(BS-NDI^{2-})$ exhibiting thermal stability up to 850 K and an electron mobility of 0.22 cm^2 V^{-1} s^{-1} at 298 K.[78] The more structurally flexible propionate-substituted NDI dianions (PS-NDI^{2-}) form a series of crystals of hydrated $(M^+)_2$(PS-NDI^{2-})(H$_2$O)$_n$, with $M^+ = Li^+$, Na^+, K^+, Rb^+, and Cs^+, whose crystal structures, H_2O adsorption–desorption isotherms, dielectric constants, and electron transport properties were examined by Abe et. al (Fig. 7b).[79] A common crystal structure involving these salts was the formation of electrically conducting NDI layers and M^+~O coordination network layers, which alternated along the c-axis (Fig. 7c). Three kinds of M^+~O interactions, namely M^+~O=, M^+~$^-$OOC−, and M^+~H_2O coexisted in the 2D layer, where the reversible H_2O adsorption–desorption cycle occurred via the gate-opened H_2O sorption processes at 298 K. The H_2O adsorption–desorption property influenced the electron mobility of the NDI layer and the M^+

conductivities for small Li^+, Na^+, and K^+ cations. In general, the electron mobility was suppressed in the presence of H_2O molecules.[80] However, the electron mobility of $(M^+)_2$(PS-NDI^{2-})(H$_2$O)$_n$ salts was enhanced by the presence of H_2O molecules, facilitating the formation of H_2O-tolerant n-type semiconducting materials. In contrast, the presence of H_2O molecules drastically suppressed the ion conductivity. All the salts showed a semi-circular trace in the corresponding Cole–Cole plots, while maximum σ_{Li+}, σ_{Ns+}, and σ_{K+} values of 3.0×10^{-7}, 1.0×10^{-4}, and 3.4×10^{-5} S cm^{-1}, respectively, were observed for unhydrated crystals (Fig. 7d). The existence of H_2O molecules led to the formation of the M^+~(H$_2$O)$_n$ coordination structure, which increased the apparent ionic radius and decreased the ionic conductivity. Reversible H_2O adsorption–desorption switching behaviour was observed with respect to the electron mobility and ionic conductivity of (M^+)(PS-NDI^{2-})(H$_2$O)$_n$ crystals for $M^+ = Li^+$, Na^+, and K^+.
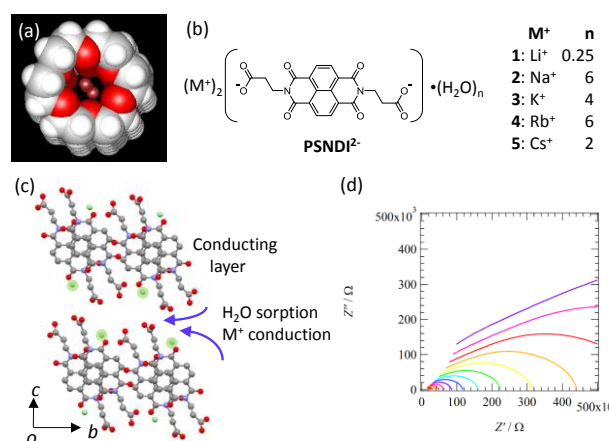

M^+	n
1: Li^+	0.25
2: Na^+	6
3: K^+	4
4: Rb^+	6
5: Cs^+	2

Fig. 7. Long-range M^+ dynamics in $[Ni(dmit)_2]$ and $(M^+)_2$(PS-NDI^{2-})(H$_2$O)$_n$ salts. (a) 1D regular array of [18]crown-6 and the formation of the dynamic Li^+ channel in $(Li^+)_x([18]crown-6)[Ni(dmit)_2]_2$ crystals. (b) $(M^+)_2$(PS-NDI^{2-})(H$_2$O)$_n$ crystals with M^+ = Li^+, Na^+, K^+, Rb^+, and Cs^+ for different H_2O amounts. (c) Schematic crystal structure of $(M^+)_2$(PS-NDI^{2-})(H$_2$O)$_n$, where the H_2O molecules indicate reversible adsorption–desorption behaviour into the 2D layer between the electrically conducting NDI layers. (d) T-dependent Cole–Cole plots of unhydrated (Na^+)(PS-NDI^{2-}) crystals. Figure modified from Ref. 79. Copyright 2021 American Chemical Society.

On the contrary, large cations of Rb^+ and Cs^+ completely suppressed the long-range ionic motions in the crystals, instead exhibiting thermally activated short-range fluctuations as two distinct Debye-type relaxation processes in the dielectric measurements.[79b] The crystal structures of these two salts were almost identical to those of Na^+ and K^+ cations within alternate layers of electrically conducting NDI and inorganic M^+~O layers. In contrast with small cations, large and heavy cations formed a rigid crystal lattice, which was consistent with the substantially higher relative pressure for the gate-opened H_2O adsorption behaviour. The rigid crystal lattice and highly polarised Rb^+ and Cs^+ cations increased the electron mobility, in contrast with those of Na^+ and K^+ salts. The systematic modification of M^+ in PS-NDI^{2-} salts adjusted the lattice softness and hardness with respect to cation–anion electrostatic Coulomb interactions, thus affecting the electron mobility. The reversible H_2O adsorption–desorption cycle at the M^+ sites was

observed in the crystal lattice, which featured tight electrostatic bonding.

5. Dynamics of molecules

Both H^+ and M^+ dynamics play an important role in the chemical design of ferroelectricity and ion conductivity, whereby structural units can coexist in electrically conducting molecular crystals to couple with dynamic motions and conduction electrons. However, fabricating molecular assembly environments that promote molecule dynamics has traditionally been more difficult. For example, it is difficult to achieve long-range diffusion using large molecules, although rotational dynamics can be introduced into the molecular assembly. The complicated, functional molecular assemblies found in biological systems are dynamic, non-equilibrium systems, and require a continuous supply of external energy to maintain the structure. Such biological systems cannot be fabricated using current synthetic approaches. One potential starting point is the fabrication of artificial molecular rotators that can be coupled with the physical properties of molecular assemblies.

5. 1. Molecular rotation

The dynamic behaviours of molecules in solids have been examined in spherical, rod-like, and disc-shaped molecules such as AD, C_{60},[20] n-alkanes,[27] and pyrene complexes,[28] where they behave as plastic crystals. However, owing to their physical and chemical properties, these dynamic molecular assemblies are almost inert. Recently, polar ionic plastic crystals have been utilised as ferroelectrics,[81,82] while coupling phenomena between dielectric, magnetic, and optical properties have been observed in polar N-oxyl-AD (NOAD) neutral radical crystals at approximately 300 K.[83] The formation of the singlet spin and antiferroelectric ground state of NOAD crystals can be thermally activated to form paramagnetic and paraelectric states via molecular rotation and breaking in NOAD pairs. Using molecular design to synthesise dynamic plastic crystals is an interesting approach for fabricating multifunctional molecular materials. In addition, the supramolecular approach is a powerful technique for forming dynamic environments in the highly ordered single-crystalline phase.[71]

Disc-shaped molecules bearing long alkyl chains can appear as discotic columnar liquid crystal phases,[30] whereas disc-shaped π-molecules, such as binary pyrene complexes, also form a thermally activated in-plane molecular rotator phase in the π-stacking column.[28] Herein, we focused on the formation of the polar in-plane rotator phase of dibromoiodo-mesitylene (DBIM) crystals[84] in the π-stacking columnar structure. To elucidate the mechanism of in-plane dipole rotation, non-polar tribromo- mesitylene (TBM) was compared with polar DBIM (Fig. 8a). Both DBIM and TBM formed a similar π-stacking columnar structure, and first-order phase transitions were observed at 358 and 298 K in the second heating cycle. The low-T and high-T phases correspond to the static-ordered crystal phase and the thermally activated disordered rotator

phase, respectively. The in-plane rotation of DBIM molecules induces slight changes in the dipole moment, which can be detected by dielectric measurements, while the in-plane rotation of TBM is inert and does not affect the in-plane dipole moment. The singe crystal X-ray structural analysis of DBIM at 100 K revealed static orientational disorder in the Br and I groups in an average molecular structure overlapping Br and I positions, which changes to the dynamic in-plane rotation phase above 358 K.

Changes in the birefringence and domain structure were confirmed via POM images after the phase transition to the rotator phase, phenomena typically observed in the order–disorder phase transition of plastic crystals. Ferroelectricity was not observed in the low-T phase of the DBIM crystal, and the high-T rotator phase corresponds to the paraelectric phase. Therefore, the phase transition in DBIM crystals is an antiferroelectric–paraelectric phase transition; however, the T- and f-dependent dielectric constants of DBIM crystals are not consistent with typical behaviour. To understand this inconsistency, collective in-plane molecular rotation, which was instigated by intermolecular I•••I interactions, was applied in the 1D π-stacking column. However, collective rotation in one molecular assembly column is independent to each other, suggesting a random rotation overall. Therefore, unidirectional molecular motors were not obtained in DBIM crystals. The chemical design of the rotator unit enables the formation of the collective rotary mode, which is important for realising unidirectional molecular motor in molecular assembly.
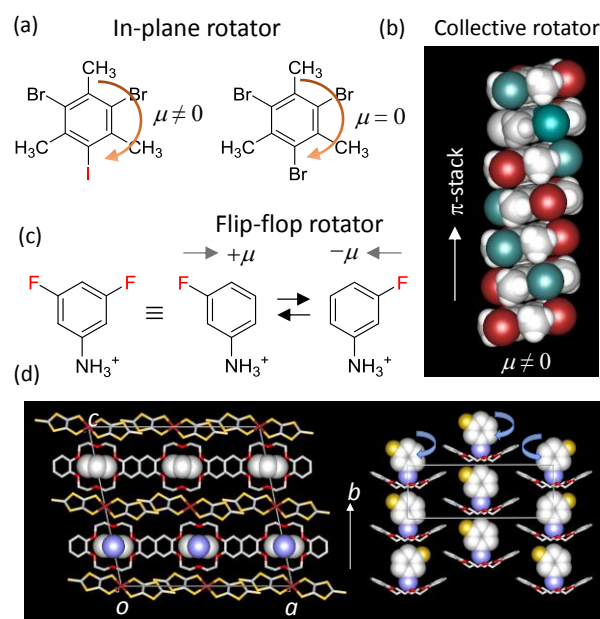

Fig. 8. Collective and polar molecular rotators. (a) In-plane molecular rotators of DBIM and TBM, where the in-plane dipole moment is observed in the DBIM molecule. (b) Collective in-plane rotation of DBIM in the π-stacking columnar structure, which occurs with the aid of effective I•••I interactions. (c) Flip-flop dipole rotator of m-FAni$^+$ in m-FAni$^+$(DB[18]crown-6)[Ni(dmit)$_2$]$^-$ crystals. The average structure was observed in the X-ray structural analysis. (d) Unit cell viewed along the b axis (left) and 2D arrangement of m-FAni$^+$(DB[18]crown-6).

Molecular dynamics are introduced into single crystals using a supramolecular approach. Solid-state molecular dynamics

have been reported in molecular turnstiles and gyroscopes,[85] and many molecular gyroscopes have been developed in the covalently bonded molecules of the rotator–stator structure by Garcia-Garibay et al.[86] Furthermore, we have reported supramolecular rotators of large club-sandwich-type supramolecular cations of $Cs^+_2([18]crown-6)_3$ in $[Ni(dmit)_2]^-$ crystals, in which the molecular rotation affects the T-dependent magnetic susceptibility of $[Ni(dmit)_2]^-$ π-dimers.[38] The rotational dynamics of disc-shaped [18]crown-6 molecules was confirmed by T-dependent solid-state ^1H NMR and ^{133}Cs NMR spectra, where the in-plane rotation of large $Cs^+_2([18]crown-6)_3$ supramolecules was insufficient to modulate the occupancy volume in the unit cell. However, the molecular rotation modulates the crystal lattice and the magnitude of the intermolecular magnetic exchange energy between $[Ni(dmit)_2]^-$ anion radicals through the two $S = 1/2$ spins, which corroborates the T-dependent magnetic susceptibility.

Simple supramolecular $Ani^+([18]crown-6)$ cations were identified in $[Ni(dmit)_2]^-$ crystals, where they serve as dynamic dual-rotator structures with the Ani^+ and [18]crown-6 components exhibiting different rotation speeds, as evidenced by T-dependent solid-state ^1H NMR and ^2H NMR spectra.[45] In addition, according to single-crystal X-ray structural analyses and theoretical calculations of the potential energy curves, the Ani^+ and $AD-NH_3^+$ rotators demonstrated two- and three-fold rotational symmetry, respectively.[44] Replacing the disc-shaped [18]crown-6 with the bulky DB[18]crown-6 and dicyclohexyl[18]crown-6 led to the formation of rotator–stator supramolecular structures in $[Ni(dmit)_2]^-$ crystals.[87] This supramolecular cation approach is a conventional and easy to implement design approach for fabricating various types of solid-state rotator–stator structures. Symmetrical rotators with an invariant dipole moment yield an inert dielectric response. Therefore, we designed polar rotator units ranging from Ani^+ to the polar m-$FAni^+$ cation in m-$FAni^+(DB[18]crown-6)[Ni(dmit)_2]^-$ crystals.[88] The 2D layer structure of rotator – stator unit of m-$FAni^+(DB[18]crown-6)$ and magnetic $[Ni(dmit)_2]^-$ arrangement was alternatively elongated along the c axis (Fig. 8d). The disordered orientation of F-group of m-$FAni^+$ was observed in the structural analysis, and the one m-$FAni^+$ cation was surrounded by four DB[18]crown-6 and two nearest neighbouring $[Ni(dmit)_2]^-$ anions along the c axis. Therefore, the potential energy curve for the rotation of m-$FAni^+$ was dominated by the two $[Ni(dmit)_2]^-$ anions. Both the T- and f-dependent dielectric constants revealed a dielectric peak at 356 K, which was not clearly observed in the isostructural crystals of $Ani^+(DB[18]crown-6)[Ni(dmit)_2]^-$. The flip-flop rotation of polar m-$FAni^+$ cations gave rise to a distorted $P–E$ hysteresis curve, where the leak current of the electrically conducting $[Ni(dmit)_2]^-$ salt (~1 $MΩ\ cm^{-1}$) disturbed the ideal $P–E$ response. Therefore, the dynamic two-fold molecular inversion of the polar m-$FAni^+$ cation is the origin of the ferroelectric behaviour (Fig. 8c). The single-

crystal X-ray structural analysis at 100 K indicated a disordered F-orientation at both the left and right sides of the m-$FAni^+$ cations, with a non-equivalent occupation factor of 0.6:0.4 for the as-grown single crystals. However, after the phase transition to the paraelectric phase, this occupation factor changed to an equivalent value of 0.5:0.5, while the poling process of single crystals in the paraelectric phase, together with cooling to 298 K, changed the occupation factor to the non-equivalent ratio of 0.7:0.3, thereby suggesting that the application of E_{out} and the ferroelectric ground state of m-$FAni^+(DB[18]crown-6)[Ni(dmit)_2]^-$ single crystals induces the dynamic rotation of m-$FAni^+$ cations. The molecular dynamics of m-$FAni^+$ cations are associated with macroscale ferroelectric properties. In general, the closet packing structure in single crystals disappears within the molecular rotation space, where the use of a supramolecular cation approach is useful for designing a dynamic environment for the polar rotator. Solid-state molecular rotators are a useful starting point for obtaining artificial molecular motors in molecular assemblies.

5. 2. Inversion of polar alkylamide chains in liquid crystals

Conventionally, dynamic motional freedom is observed in the rotation of the director in liquid crystal phases, and relatively large dynamic structural units can coexist in liquid crystals.[29,30] We focused on polar alkylamide ($−CONHC_nH_{2n+1}$) chains as a dynamical structural unit to design physical properties. These chains were combined with π-molecular systems, such as benzene, pyrene, and tetrabenzoporphyrin, to fabricate ferroelectric liquid crystalline materials.[89] The usefulness of alkylamide chains in stabilising the discotic hexagonal columnar (Col_h) liquid crystal phase has been discussed by Matsunaga et al., who described their formation via N−H•••O= hydrogen-bonding interactions in the original liquid state.[90] The 1D N−H•••O= hydrogen-bonding chains along the π-stacking column generate a macroscale dipole moment along the column direction, which can be inverted by the application of E. In the Col_h phase, the lateral $–(CH_2)_nCH_3$ alkyl chains are completely melted, while the formation of N−H•••O= hydrogen-bonding interactions plays an important role in forming molecular assemblies in the Col_h phase. The Col_h phase and the formation of organogels have previously been reported in a 1,3,5-alkylamide-substituted benzene derivative (3BC),[91] while ferroelectric $P–E$ hysteresis behaviour in the Col_h phase was first reported by Sijbesma et al.[92,93] We also examined the 1,4-, 1,2,4,5-, 1,2,3,4,5-, and 1,2,3,4,5,6-alkylamide-substituted benzene derivatives (2BC, 4BC, 5BC, and 6BC) in terms of molecular assembly structure, dielectric response, organogellation ability, and ferroelectric properties.[93] Among them, 2BC, 3BC, and 5BC showed ferroelectric behaviour, where the steric hindrance of the rotation of the neighbouring N−H•••O= hydrogen-bonding sites is a key point in realising dipole inversion and ferroelectricity.
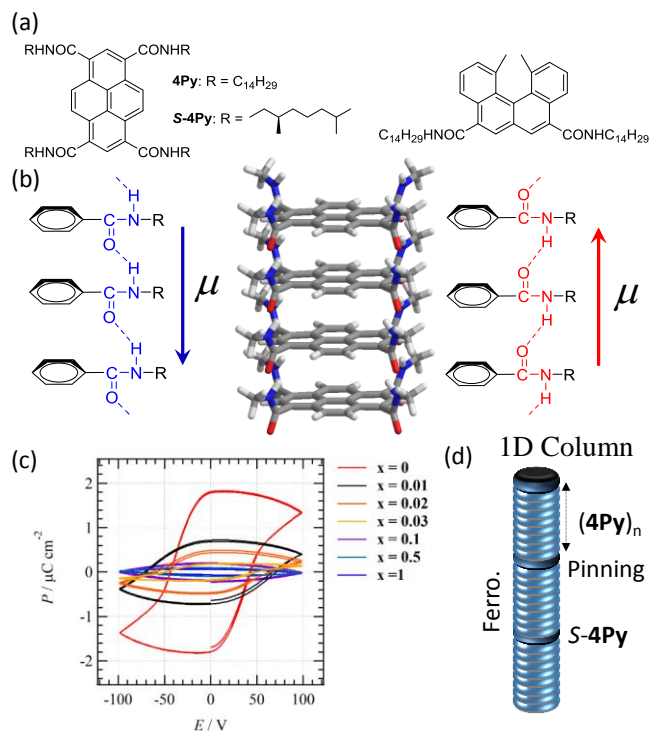
Fig. 9. Dynamic motion of N−H•••O= hydrogen-bonding alkylamide chains in liquid crystals. (a) Molecular structures of alkylamide-substituted pyrene (4-Py) and helicene (HC) derivatives. (b) Hydrogen-bonding N−H•••O= amide chains along the π-stacking direction and the inverted form necessary for ferroelectric behaviour. (c) Doping effect on $P–E$ hysteresis curves when chiral S-4Py is inserted into the ferroelectric 1D column of 4-Py. (d) Schematic model of the doping state of S-4Py and the formation of the pinning potential in the 1D ferroelectric column. Figure modified from Ref. 97. Copyright 2019, Wiley −VCH Verlag GmbH & Co. KGaA.

The systematic evaluation of benzene derivatives clarified a design strategy for ferroelectricity, which enabled the design of multifunctional physical properties based on the π-extended pyrene core. Significant research has been devoted to the study of pyrene derivatives, with blue monomer and green excimer emissions typically observed in the concentration-dependent emission spectra in the solution phase.[94] At temperatures above 295 K, the Col_h liquid crystal phase exhibited four −$CONHC_{14}H_{29}$ chains in the pyrene π-core (4Py), which affected the $P–E$ hysteresis curve (Fig. 9c).[95] In the Col_h phase, 1D N−H•••O= hydrogen-bonding π-stacking columns are arranged hexagonally, and the application of E inverts the polarisation direction (Fig. 9b). The remanent polarisation (P_r) and coercive electric field (V_{th}) of the ferroelectric $P–E$ hysteresis curve of 4Py at 453 K were 1.79 μC cm^{-2} and 1.5 V μm^{-1}, respectively, at f = 0.1 Hz. These values were similar to those of 3BC at 343 K (P_r = 0.8 μC cm^{-2} and V_{th} = 25 V μm^{-1}, respectively, at f = 0.1 Hz).[92] The formation of the hydrogen-bonding aggregate of $(4Py)_n$ was observed in solution phase, where monomer–excimer emission conversion was observed at a considerably lower concentration (10^{-6} M) than that of pyrene itself (10^{-3} M).[96]

In contrast, chiral alkylamide-substituted S-4Py showed circular polarised luminescence behaviour at g factor of g_{lum} ~ 0.03 in methylcyclohexane, implying the formation of a highly

ordered chiral π-stacking aggregate.[96] However, the chiral S-4Py structure did not exhibit the Col_h phase or ferroelectric properties. Therefore, we prepared mixed crystals comprising both ferroelectric 4Py and chiral, non-ferroelectric S-4Py in order to examine the ferroelectric correlation length in the 1D column.[97] Bulky S-4Py molecules were inserted at random into the 1D ferroelectric hydrogen-bonding column of $(4Py)_\infty$ to create the pinning potential required for dipole inversion. An S-4Py doping concentration of just 3% was sufficient to suppress ferroelectric behaviour (Fig. 9c), suggesting a correlation length of 12 nm for the ferroelectric π-stacking $(4Py)_{33}$ via each S-4Py (Fig. 9d). Similarly, mixed crystals consisting of ferroelectric 3BC and antiferroelectric 4BC, $(3BC)_{1-x}(4BC)_x$, have been examined in the Col_h phase, where both molecules can form the same Col_h liquid crystal phase.[98] The ferroelectric correlation length of 3BC, in response to 3% doping of 4BC, was approximately 12 nm. For 1D columnar systems, a ferroelectric correlation length of 12 nm is typical for the possible dipole inversion of N−H•••O= hydrogen-bonding interactions between the $CONHC_{14}H_{29}$ chains.

The application of E along the π-stacking direction of the Col_h liquid crystal phase can invert the direction of the dipole moment and generate a local electric field (E_{loc}) along the π-stack of 4Py. The current–voltage ($I–V$) characteristics of the π-stacking 4Py column depend on the direction of $±E_{loc}$, where $E + E_{loc}$ and $E − E_{loc}$ modulate the I value.[95] Consequently, current-switching phenomena have been observed in the ferroelectric dipole switching phenomenon. The molecular design of functional π- molecules bearing alkylamide chains is a conventional procedure for synthesising multifunctional dynamic molecular assemblies.

This concept can be expanded to the other novel π-molecular systems containing the non-planar dimethyl-helicene (HC) π-core to obtain ferroelectric molecular assemblies (Fig. 9a).[99] The Col_h liquid crystal phase gives way to the 2D lamellar liquid crystal phase in racemic HC derivatives bearing two –$CONHC_{14}H_{29}$ chains (2HC) at 330 < T < 424 K. The density of hydrogen-bonding sites in the 2D lamellar structure far exceeds that of the 1D columnar structure, leading to excellent P_r responses compared to those of the 1D system. The P_r- and E_t-values of racemic 2HC at 413 K and f = 0.5 Hz were 11.1 μC cm^{-2} and 20 V μm^{-1}, respectively, with the P_r-value of 2HC two and twelve times larger than of the corresponding values for 3BC and 4Py, respectively. However, the V_{th} value for 2HC is much larger than that of the 1D system. It should be noted that there was no poling process in the 2D hydrogen-bonding assembly owing to the well-oriented domains associated with ferroelectric $P–E$ hysteresis. Therefore, 2D hydrogen-bonding molecular assemblies are good candidates for high-performance ferroelectric materials, and the chemical design of intermolecular hydrogen-bonding interactions is a useful approach to control ferroelectric properties.

5. 3. Bowl-to-bowl inversion

Several dynamic molecular assembly variants have been designed in which the motional freedom is accompanied by a

double-minimum type potential energy curve, giving rise to ferroelectric behaviour. For instance, the bowl-inversion of non-planar π-molecules is one interesting approach for designing ferroelectric molecular assemblies. Alternatively, non-planar π-molecules such as sumanene and corannulene have attracted considerable attention as partial structural units for the preparation of C_{60}.[100,101] The bowl-to-bowl inversion of sumanene occurred in the solution phase, which activation energy was approximately 18.2 kcal mol^{-1}.[100] Such molecular inversion is usually suppressed in closest-packing structures. We focused on the trithiasumanene (SS) molecule, replacing three peripheral –CH_2 units with S atoms, which decreased the depth of the bowl sphere and resulted in a bowl-to-bowl inversion activation energy of 1.9 kcal mol^{-1}.[102] Thermally activated bowl-to-bowl inversion in molecular assembly represents a potential avenue for creating organic ferroelectrics. Furthermore, the introduction of six –OC_nH_{2n+1} chains into the SS π-core (CnSS) enhances the flexibility of the molecular assembly and facilitates the generation of dynamic motional freedom via bowl inversion (Fig. 10a).[103]

Five CnSS derivatives with different alkyl chain lengths (n = 2, 6, 8, 10, and 16) were prepared, with their phase transition behaviours evaluated using POM and DSC measurements.[103] Notably, three compounds, C6SS, C8SS, and C10SS, showed a solid–solid (S1–S2) phase transition before melting to form an isotropic liquid (L), where the high-T phase (S2) demonstrated high viscosity and plasticity without forming a liquid crystal phase (Fig. 10b). In contrast, the longest chain derivative (C16SS) showed a Col_h liquid crystal phase after transitioning from the S2 phase.

Sharp Bragg diffraction peaks were observed in the T-dependent PXRD patterns of the crystalline S1 phase, while a diffraction pattern resembling that of the Colh phase was observed for the high-T viscous S2 phase. In the S2 phase, the (100), (110), and (200) reflection peaks were attributed to the formation of a hexagonal lattice, while a broad reflection peak representing the melting of the alkyl chains was observed at approximately 2θ ~ 20°. An average π-stacking distance of 3.5 Å at 2θ ~ 25° implied the formation of π-stacking hexagonal columnar molecular assemblies and a liquid-like melting state of the lateral alkyl chains without the formation of a liquid crystal phase. Thermally activated in-plane free rotation of the bowl-shaped molecules in the column was suppressed in the S2 phase, similar to the behaviour observed for plastic crystals. Only the C16SS derivative showed the Col_h liquid crystal phase, where the in-plane rotation of the molecules was activated to form a liquid crystal phase.

Fig. 10. Molecular structure of (a) CnSS and (b) the phase transition behaviour of C10SS together with POM images of the S1 and S2 phases.

No dielectric anomalies were detected in the T-dependent behaviour at the S1–S2 phase transition temperature, while the ε_2 peak was observed in the S2 phase before melting to form a liquid. The latter dielectric anomaly was consistent with the thermally activated motional freedom of the polar structural unit, suggesting the existence of bowl-to-bowl inversion between the lower (A) and the upper (B) bowl conformations in the 1D columnar molecular assembly (Fig. 10b). This bowl-to-bowl inversion was confirmed in the T-dependent P–E hysteresis curves (Fig. 10c). After the phase transition to the viscous S2 phase, f-dependent dielectric enhancement was thermally activated in the high-T region, which showed clear P–E hysteresis curves for the C10SS derivative at 353 K. The P_r- and E_t-values of C10SS were 0.5–0.7 μC cm^{-2} and 1.5 V μm^{-1}, respectively. The P–E hysteresis curves at f = 100 and 200 Hz displayed almost identical profiles, suggesting a bowl-to-bowl inversion frequency of several hundred hertz. To confirm the bow-to-bowl inversion mechanism, we prepared a similar shallow bowl molecule, namely C4Se, by replacing three S atoms with larger Se atoms, which decreased the bowl-depth. Furthermore, the π-planar triphenylene (C6TP) derivative was compared with the ferroelectric response of C10SS. The P–E hysteresis curve of C4Se had a low magnitude, and hysteresis behaviour was not observed in the π-planar C6TP without bowl inversion. These P–E hysteresis curves for different molecular systems were consistent with the bowl-to-bowl inversion mechanism observed for the ferroelectric CnSS molecule. Single columns of CnSS measure approximately 1 nm^2, with the application of single-column ferroelectric memory enabling organic memory devices with a high density of 12.8 Tb cm^{-2}.
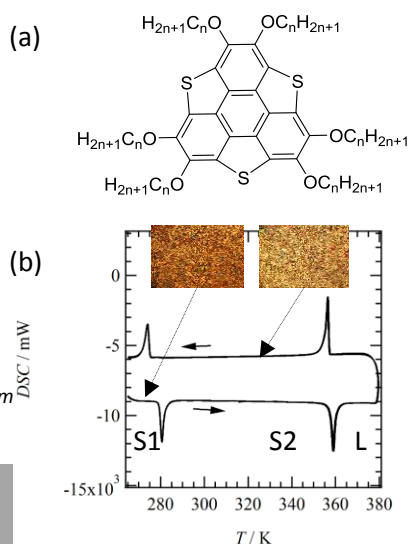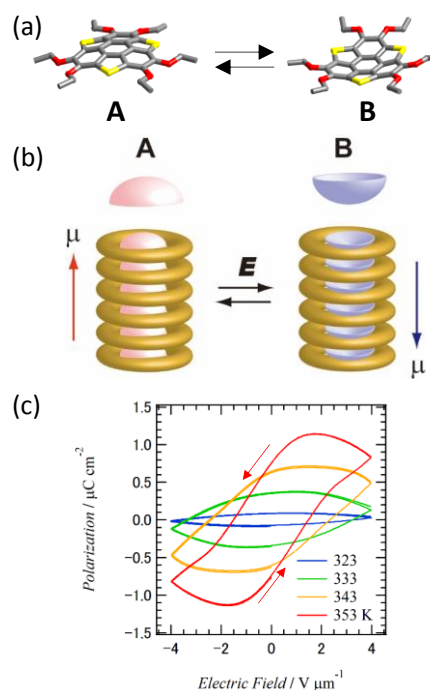

(a)

(b)

(c)

(a)

(b)

Fig. 11. Bowl-to-bowl inversion and ferroelectricity in CnSS. (a) Molecular inversion between the lower bowl (A) and the upper bowl (B). (b) Schematic representation of the polarisation inversion between the lower (A) and upper (B) bowl columns in response to applying E. (c) T-dependent P–E hysteresis curves of C10SS at f = 100 Hz.

5. 4. Dynamics and thermal conductivity

A family of organic-inorganic 2D layered compounds of the formula $(C_nH_{2n+1}NH_3)_2MX_4$ ($CnNH_3MX_4$, M^{2+} = Cu^{2+}, Mn^{2+}, Zn^{2+}, etc., X^- = Cl^- and Br^-) have been extensively studied with respect to their structural phase transitions,[104] 2D ferromagnetism,[105] and ferroelectric behaviour.[106] The molecular motions of flexible $C_nH_{2n+1}NH_3^+$ chains are thermally activated in the high-T phase, where a glassy phase emerges because of the disordered organic layers. Recently, drastic changes in the heat transport properties have been reported in the sequential phase transitions of $(C_4H_9NH_3^+)_2CuCl_4^{2-}$ ($C_4NH_3CuCl_4$) by Hoshino et al.[107] The DSC diagram of $C_4NH_3CuCl_4$ crystals shows reversible three-step phase transitions in the 176–218 K temperature range (Fig. 12a). The tilted $C_4H_9NH_3^+$ alkyl chains in the α- and β-phases change to a fully elongated state in the δ-phase, and the interlayer distances between the inorganic $CuCl_4^{2-}$ planes increased significantly.

The γ-phase is an intermediate incommensurate phase. Single-crystal X-ray structural analysis revealed third-order satellite peaks, which are characteristic of modulated incommensurate crystals.[108] The crystal structure was modelled in the $P2_1/c$ (α0γ)00 super space group, in which the $CuCl_4^{2-}$ sheets formed wave-like structures consisting of connected alternating regions of β-like and δ-like structures.
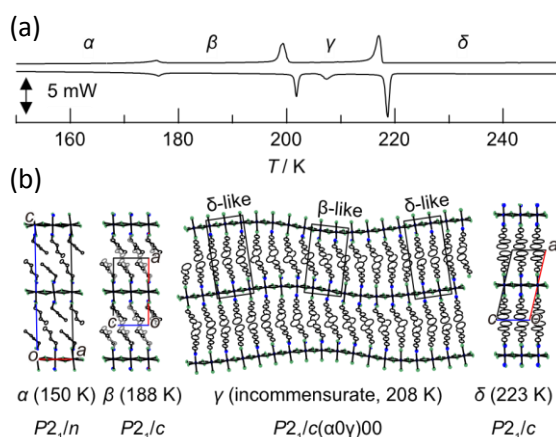

Fig. 12. Phase transition behaviour and crystal structures of $C_4NH_3CuCl_4$. (a) DSC chart spanning each phase. (b) Diagrams of α-, β-, γ-, and δ-phases viewed along the b axis (produced using ORTEP software). The grey lines in the β-phase correspond to the disordered alkyl-chains. Figure modified from Ref. 107. Copyright 2020 Wiley –VCH Verlag GmbH & Co. KGaA.
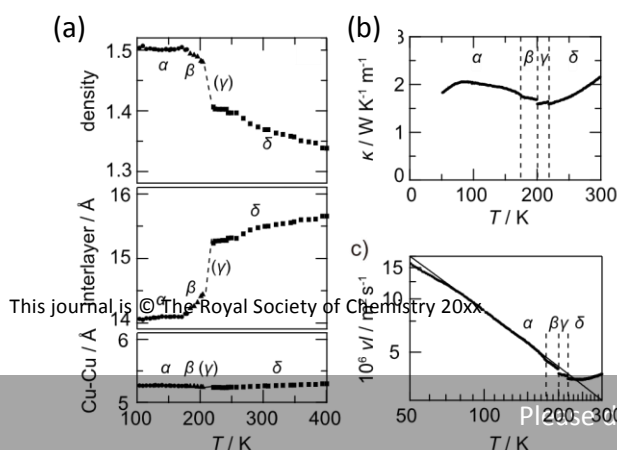

Fig. 13. Phase transition behaviours of $C_4NH_3CuCl_4$. (a) T-dependent changes of the structural parameters based on PXRD patterns. Calculated densities, distances between $CuCl_4^{2-}$ layers, and Cu–Cu distances in the $CuCl_4^{2-}$ layers. T-dependent (b) $κ$ and (c) vl for a single crystal. Figure modified from Ref. 107. Copyright 2020 Wiley –VCH Verlag GmbH & Co. KGaA.

In the γ- and δ-phases, thermal fluctuations in the $C_4H_9NH_3^+$ chains were observed in the single-crystal X-ray structural analyses. The PXRD pattern also indicated that the thermal expansion of the flexible $C_4H_9NH_3^+$ chains between the rigid $CuCl_4^{2-}$ layers was restricted (Fig. 13a). This structural environment induced glass-like thermally conducting properties. Figure 13b shows the T-dependent thermal conductivity ($κ$, W K^{-1}). Below 85 K, the $κ$ value has a positive T-coefficient because the mean free path (l) of the phonons is maximised owing to imperfections in the crystal lattice. From approximately 85–200 K, the T-coefficients became negative, which was attributed to the decrease in l for phonon scattering. This behaviour is typical in insulating crystalline materials. However, above 200 K, the T-coefficient for the $κ$ value changes to a positive value, which is typical for glassy solids, liquids, and gases.

In simple gas kinetics, $κ$ is expressed as $κ = 1/3Cvl$, where C is the heat capacity, v is the phonon velocity, and l is the phonon mean free path. In crystalline materials, l is proportional to T^{-1}, while in glassy materials, it is approximately constant.[109] The vl values based on the experimental $κ$ values and the normal heat capacity (C_p) correlate closely with a T^{-1} function (solid line in Fig. 13c) between 80 and 200 K. However, above 200 K, the vl values diverged from the T^{-1} function and became approximately constant. This behaviour corresponds to the phase transition from crystalline to glassy states, which is activated by the molecular dynamics of alkyl chains. Similar dynamic behaviour has also been observed in the T-dependent thermal conductivity measurements for order–disorder type inorganic ferroelectrics, namely $RbHSO_4$ and NH_4HSO_4.[110]

6. Dynamics of crystal lattices

The intermolecular interactions in molecular crystals vary widely, encompassing strong electrostatic, hydrogen-bonding, CT, and weak van der Waals interactions.[33] Certain hydrogen-bonding molecular crystals show reversible gas or molecular adsorption–desorption behaviour.[31] Single-crystal X-ray structural analysis, thermogravimetric analysis, and adsorption–desorption isotherm have been typically utilised the external stimuli responsible crystal lattice transformation between host and host – guest assembly. Typical molecular crystals did not exhibit reversible molecular adsorption behaviour, which expands and destroys the crystal lattice. However, the hydrogen-bonding crystal lattice is constructed with a bonding energy of 10–20 kJ mol^{-1}, and the intermolecular interaction for the guest adsorption process is dominated predominantly by weak van der Waals interactions of ~5 kJ mol^{-1} during the reversible molecular adsorption–desorption cycle. Although the dynamics of the host crystal lattice occur at much larger amplitudes than those of H^+ and M^+ dynamics, many HOF

crystals have been developed using high-performance gas adsorption materials with relatively large BET surface areas.[31,111] The structural recovery and reconstruction of HOFs is easily achieved via the recrystallisation process, which offers low-energy consumption and environmentally friendly organic functional materials. Herein, we introduce three types of hydrogen-bonding host–guest molecular crystals with 1D, 2D, and 3D networks.

6. 1. Molecular rearrangement by guest sorption

A variety of hydrogen-bonding sites have been designed using organic synthetic techniques to fabricate 1D, 2D, and 3D hydrogen-bonding supramolecular assemblies.[112] For example, 1D hydrogen-bonding channels have been reported in bisurea-macrocycle (BIUM) derivatives,[113,114] while 2D networks have been confirmed in 2,5-DABT[115] and $(G)_2(BDS^{2-})$ structures,[116,117] where G and BS^{2-} are guanidinium and 1,4-benzene-bisulfonate, respectively (Fig. 14). These hydrogen-bonding molecular assemblies show reversible gas (N_2 and CO_2) and adsorption–desorption behaviours for pyridine (Py), benzonitrile (PhCN), piperidine (Pipe), DMF, THF, 1,4-dioxane (Diox), CH_3OH, aniline (Ani), coumarin (Coum), nitrobenzene ($PhNO_2$), hexamethylenetetramine (HMTA), and quinoline (Quino), accompanied by the crystal lattice transformation of the host framework.[114,115,117]

Two N−H•••O= hydrogen-bonding sites in the BIUM molecule formed a regular 1D array and a channel via the recrystallisation of acetic acid (AcOH),[113,114] where the AcOH molecules were within the channel to form 1:1 host–guest molecular crystals. Photo-polymerisation reactions have been examined for use within the crystalline space of the channel.[113] The guest AcOH molecules inside the channel can be removed by thermal treatment at 450 K, with the N_2 molecules introduced into the channel space by cooling to 298 K (Fig. 15a). Reheating the empty channel to 510 K transformed to the zigzag 1D stack to minimise the empty vacuum space in the crystal. The vapour diffusion of pyrrole (Pyr), Py, and 2,3-difluoroaniline (F2-Ani) to form zigzag channels rearranged the crystal structure of the host–guest molecular crystals, and the guest molecules were reversibly removed using thermal treatment. The zigzag structures were again transformed to the structure of the channel after the vapour diffusion of AcOH. The reversible structural transformation between the 1D and zigzag channels was realised by the stepwise procedure of thermal treatment, guest adsorption, thermal annealing, and vapour diffusion of AcOH. From the N_2 and CO_2 adsorption – desorption isotherms, the N_2 molecule can only pass through the 1D channel without the sorption of CO_2. Neither N_2 nor CO_2 can pass through the small void space zigzag structure.
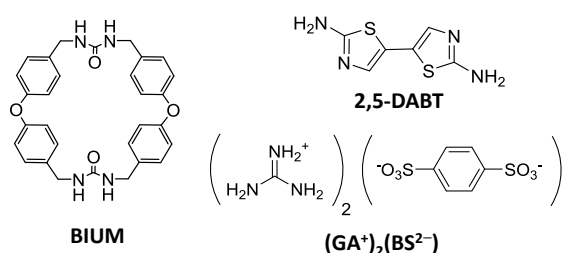
Fig. 14. Molecular structures of the 1D and 2D hydrogen-bonding systems of the BIUM, 2,5-DABT, and $(G^+)_2(BS^{2-})$ frameworks.

Although H^+ conductivity has been reported in (2,5-$H2DABT^{2+}$ salts with $H_2PO_4^-$,[62] neutral 2,5-DABT can form a variety of hydrogen-bonding host–guest molecular crystals involving guest molecules of Py, PhCN, Pipe, DMF, THF, Diox, CH_3OH, Ani, Coum, $PhNO_2$, HMTA, and Quino.[115] Moreover, reversible guest adsorption–desorption cycles have been observed in relatively small guest molecules, where the reversible transformation of the N−H•••N hydrogen-bonding host crystal lattice is observed during the sorption of highly crystalline guests. Two kinds of hydrogen-bonding sites, namely −NH$_2$ groups and the ring nitrogen of the thiazole (Thz) ring, can contribute to the formation of host hydrogen-bonding lattices (Fig. 15b). The vapour adsorption of Py molecules into a host 2,5-DABT lattice formed single crystals of (2,5-DABT)(Py)$_2$, where the guest Py molecules were inserted in the space between the 2D layers of hydrogen-bonding 2,5-DABT. A slight change in the orientation of the 2,5-DABT molecules occurred in the 2D layer, thereby generating an adequate crystalline space for guest adsorption. The Py molecules were reversibly removed by thermal annealing in the highly crystalline state, while Py re-adsorption was observed by the vapour diffusion of Py. The reversible adsorption–desorption cycle for highly crystalline Py guests was observed (Fig. 15c). Similar structural transformations have been observed in the molecular adsorption of Pipe, DMF, Diox, and PhCN.[115] Dynamic crystal lattice transformation according to the guest molecules occurs owing to the energy consumption of the hydrogen-bonding crystal lattice and the weak bonding of guest molecules to the host lattice through van der Waals interactions. In the case of 2,5-DABT, interlayer van der Waals interactions can easily open space for guest adsorption.
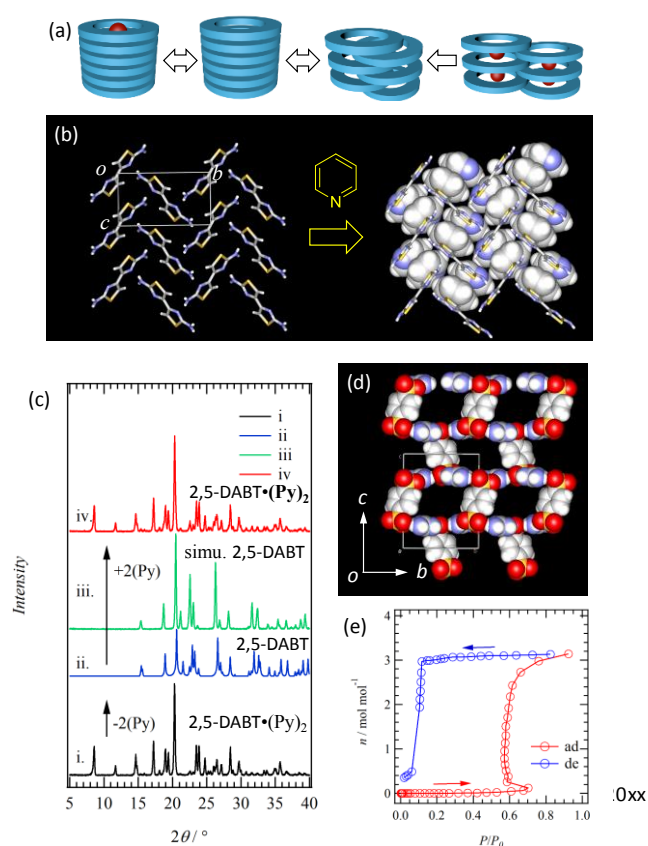

(a)

(b)

(c) 2,5-DABT•(Py)$_2$ / simu. 2,5-DABT / 2,5-DABT / 2,5-DABT•(Py)$_2$

(d)

(e)

2,5-DABT

BIUM

$(GA^+)_2(BS^{2-})$

Fig. 15. 1D and 2D hydrogen-bonding host–guest molecular crystals. (a) Formation of various types of 1D molecular assemblies of BIUMs. (b) 2D hydrogen-bonding layer of 2,5-DABT and its structural transformation by Py adsorption. (c) The desorption – readsorption cycle of host-guest crystals 2,5-DABT•(Py)₂. PXRD patterns of i) as-grown crystals 2,5-DABT•(Py)₂, ii) Py desorption crystals 2,5-DABT after the thermal treatment at 370 K, iii) simulation pattern of 2,5-DABT based on the single crystal X-ray analysis, and iv) Py re-adsorption crystals 2,5-DABT•(Py)₂ at room temperature. (d) The electrostatic $-NH_2^+ \cdots^- SO_3-$ hydrogen-bonding layer of a $(G^+)_2(BDS^{2-})$ host with a CPK representation, where the guest adsorption space exists in the host lattice. (e) Adsorption–desorption isotherm of THF for $(G^+)_2(BDS^{2-})$ at 298 K. Figure modified from Refs. 115 and 117. Copyright 2019 and 2021 Royal Society of Chemistry and the American Chemical Society.

The energy of electrostatic hydrogen-bonding interactions is far higher than that of neutral hydrogen-bonding interactions, which enhances the stability of the host crystal lattice. The rigid $(G^+)_2(BDS^{2-})$ host lattice in which electrostatic $-NH_2^+ \cdots^- SO_3-$ hydrogen-bonding interactions form various host–guest single crystals involving H_2O, Pyrr, pyrazine (Pyz), thiophene (TP), Py, Diox, and Ani was discovered.[116,117] The crystal formula of $(G^+)_2(BDS^{2-}) \cdot (Guest)_x$ (where x = 1, 2, or 3) was observed according to the size of the guest molecule. The guest molecules were inserted into the pores between the 2D layers comprising the pillared $(G^+)_2(BDS^{2-})$ electrostatic lattice (Fig. 15c). As the initial $(G^+)_2(BDS^{2-})$ crystal contained no voids, the guest adsorption-induced transformation to form pillared crystal structures is key. The electrostatic interactions of the host crystal lattice maintain the pillared crystal lattice after guest adsorption, while weak van der Waals interactions between the host lattice and the guest molecules form dynamic host–guest molecular crystals. The reversible guest adsorption–desorption cycle into the host lattice has also been confirmed in the gate-opened adsorption–desorption isotherms for THF and benzene (Fig. 15d).[117] The thermal stability of the rigid $(G^+)_2(BDS^{2-})$ host lattice was higher than those of the 1D channel of BIUM and the 2D layer of 2,5-DABT.[114,115] The low-molecular-weight hydrogen-bonding molecular crystals can form a unique dynamic host lattice that shows a reversible molecular adsorption–desorption cycle for diverse guest molecules; in particular, electrostatic hydrogen-bonding interactions facilitate the generation of dynamic, rigid host crystal lattices. In addition, energy variations between the molecules in solids should it be the formation of interesting dynamic crystal lattice that regulates external stimuli such as molecular adsorption.

6. 2. Dynamic Hydrogen-Bonded Framework

Functional HOFs have attracted significant attention for their potential applications in gas sorption, separation, and catalysis.[118] Although the design of dynamic organic frameworks has been geared primarily toward the above technological applications, these dynamics are also utilised in the development of bulk physical properties. However, the reports on mechanically responsive molecular crystals, including thermo-responsive and light-responsive crystals, are comparatively limited.[119] Rigid and static molecular crystals with closest-packing structures are less open to structural distortion, which hampers the development of thermo-responsive molecular crystals. The thermosalient effect is a thermo-responsive phenomenon that induces a mechanical force owing to the response to an external thermal stimulus.[120] However, there are few thermosalient active crystalline materials. To explore the potential application of such

materials, new thermosalient molecular crystals must be discovered, and their underlying mechanisms require clarification in order to establish an appropriate design strategy. In our study on dynamic aromatic molecular systems,[121] we found that HOF crystals with twisted dynamic π units of tetra[2,3]thienylene tetracarboxylic acid ([2,3]ThTCA) demonstrated a thermo-responsive jumping behaviour, which was triggered by specific structural changes in the twisted π structure (Fig. 16a).[122]

The connection of twisted π-units of [2,3]ThTCA by symmetric hydrogen-bonding –COOH groups results in a unique HOF structure. The hydrogen-bonding network of the saddle-shaped [2,3]ThTCA scaffold forms a 3D supramolecular structure. Six discrete molecules formed six-membered rings, which were connected to each other (Fig. 16b). The diamond-like structure of [2,3]ThTCA was constructed using a fully fused π-system and a highly twisted tetra[2,3]thienylene π-node, closer to a regular diamondoid structure. The spatial structure and periodicity of the [2,3]ThTCA framework (2.36×2.21 nm²) lead to six-fold interpenetration of the diamond layers with stacked dynamic π units along the a axis. The molecular assembly of [2,3]ThTCA produces 1D rhombic channels (approximately 5.6×9.8 Å²), which run parallel to the a axis and facilitate the accommodation of solvent molecules by providing permanent porosity. The surface area and pore size corresponding to the N_2 isotherm are 465 m² g⁻¹ and 6.52 Å, respectively.
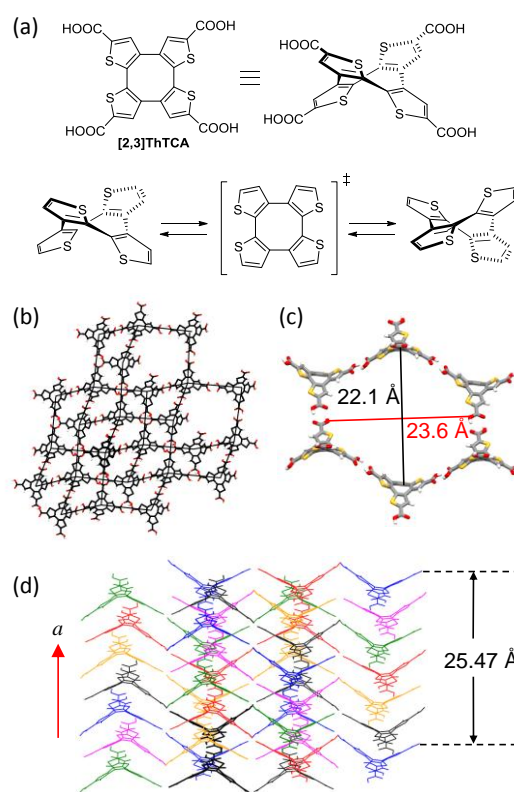

Fig. 16. Diamondoid structure and its interpenetration assembly of [2,3]ThTCA. (a) Molecular structure of [2,3]ThTCA and its structural features. (b) Diamondoid structure formed by the hydrogen-bonding assembly of [2,3]ThTCA. (c) Six-membered ring of the diamondoid substructure. (d) Six-fold interpenetration assemblies of the diamondoid structure leading to the formation of the HOF

assembly of [2,3]ThTCA. Figure modified from Ref. 122. Copyright 2019 Wiley–VCH Verlag GmbH & Co. KGaA.

The most striking feature of the [2,3]ThTCA crystals was the observation of thermo-responsive crystal jumping behaviour. Upon heating the single crystals, the birefringence of the crystal changed at approximately 400–420 K, followed by the crystal jumping phenomenon. This behaviour was triggered by THF desorption from the 1D channel. The removal of guest THF generated additional space in the host crystal lattice required for the transformation to a stable crystal form. The cooperative anisotropic motion of each molecule released stress, thus generating mechanical force and inducing the crystal jumping behaviour. The newly formed narrower void space was filled with H_2O molecules to stabilise the molecular assemblies. There are no previous reports of organic frameworks that can produce mechanical force based on the dynamic motion of the host lattice caused by guest-molecule desorption. This system offers a pathway to designing thermally stable thermosalient molecular materials, with the origin of the thermosalient behaviour clearly deriving from collective molecular motion in the molecular assemblies.
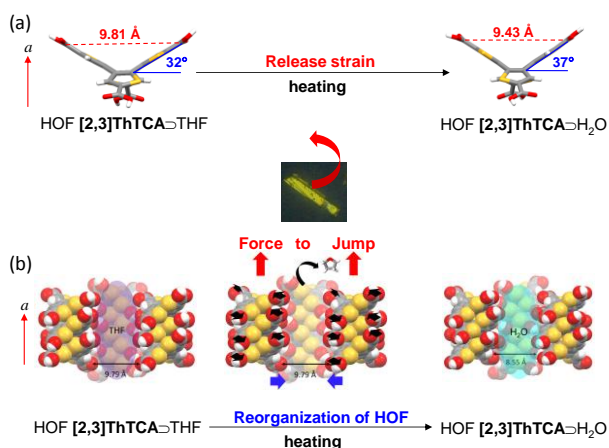

Fig. 17. Molecular mechanism of the crystal jumping in HOF [2,3]ThTCA⊃THF. (a) Significant changes in the molecular structure of the tetra[2,3]thienylene π-core from HOF [2,3]ThTCA⊃THF (before jumping) to HOF [2,3]ThTCA⊃H₂O (after jumping). The cooperative molecular motion of [2,3]ThTCA triggered by the removal of THF produces the mechanical force requisite for crystal jumping. Figure modified from Ref. 122. Copyright 2019 Wiley –VCH Verlag GmbH & Co. KGaA.

6. 3. Conformational change by molecular sensing

Structural transformation of the host crystal lattice is sometimes accompanied by an interesting physical response associated with guest adsorption. For instance, the physical properties of the electrical conductivity, dielectric constant, and emission behaviour have the potential to be modulated in host–guest

molecular crystals via external stimuli. We focused on the dynamic crystal lattice of solid-state ESIPT fluorescent chromic materials for molecular sensing, where the intramolecular PT from enol (−OH) to keto (=O) isomers showed a large Stokes shift of approximately 10,000 cm^{-1} owing to guest adsorption.[123] The 2-(2'-hydroxyphenyl)benzothiazole (HBT) molecule is a well-known solid-state ESIPT compound in which the intramolecular O–H•••N hydrogen-bonding conformation shows the intramolecular PT process in the excited state. This phenomenon has been observed in non-polar solvents, such as $CHCl_3$, or in the solid state. However, the HBT crystal lattice did not exhibit dynamic behaviour in the absence of external-stimuli responsive units. Herein, we designed a highly acidic HBT molecule bearing the −SO₃H group (SHBT) as an external-stimuli responsive unit for the detection of basic molecules (Fig. 18a), resulting in a dynamic host lattice and ESIPT fluorescent chromic behaviour.[124] The guest recognition abilities of SHBT drastically changed the ESIPT fluorescence behaviour, and the thermal annealing of the host–guest crystals removed the guest molecules and recovered the initial state. The vapour diffusion of guest molecules reversibly recovered the highly crystalline state of the host–guest crystals. The conformational isomer of the intramolecular O−H•••N hydrogen-bonding structure (trans-isomer of SHBT) showed strong green-coloured ESIPT fluorescence, while weak blue-coloured non-ESIPT fluorescence was observed in the non-hydrogen-bonding cis-isomer (Fig. 18a). The structural conversion of SHBT between these two isomers dominated the guest adsorption-induced ESIPT fluorescent response.

Although the solid-state HBT itself showed strong green-coloured ESIPT fluorescence, the solid-state SHBT was almost inert regarding the fluorescence response.[123] Single-crystal X-ray structural analysis of SHBT clarified the zwitterionic molecular structure comprising −SO₃⁻ and a thiazolium-ring after the PT process from −SO₃H to the thiazole-ring (Fig. 18b). Interestingly, the non-fluorescent SHBT drastically changed to a strong green-coloured ESIPT fluorescent state after the vapour diffusion of guest base molecules such as Py, Ani, Quin, and thiazole (Fig. 18b). Single-crystal X-ray structural analysis of (SHBT)(Py) revealed the formation of the intermolecular H⁺-transferred (HPy⁺)(SHBT⁻) salt from the highly acidic −SO₃H to the basic N-site of Py, where the N–H⁺•••⁻O₃S– hydrogen-bonding interactions dominated the intermolecular interactions. In addition, the intramolecular O–H•••N hydrogen-bonding conformation was consistent with the ESIPT active molecular structure after guest adsorption. Changing the molecular structures of Py, Ani, and Quin to thiazole slightly modulated the ESIPT fluorescent colours, suggesting molecular sensing properties.
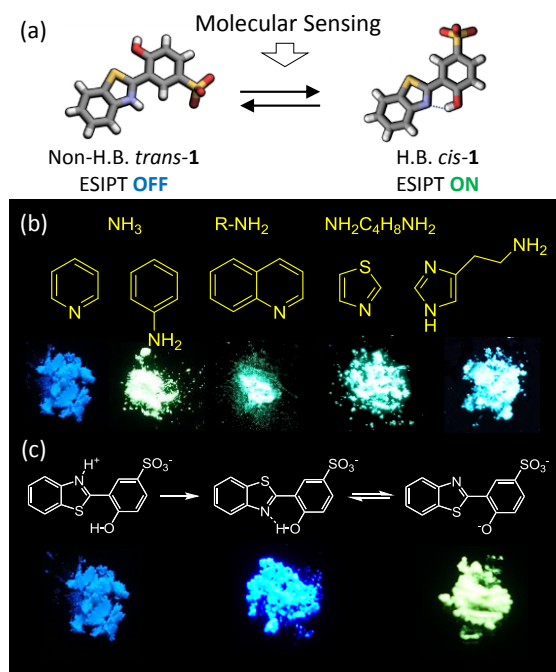
ARTICLE

Fig. 18. Fluorescent ESIPT chromic molecule of SHBT. (a) Structural transformation between non-ESIPT (ESIPT) trans-conformer without (with) an intramolecular O−H•••N hydrogen-bonding structure. (b) ESIPT fluorescence responses of SHBT for various aromatic bases. (c) Two-step ESIPT chromism for NH_3 and $C_3H_7NH_2$ and the formation of monoanionic and dianionic states. Figure modified from Ref. 123 Copyright 2018 American Chemical Society.

The neurotransmiter molecule of hystamine was also detected by the ESIPT fluorescent chromism from non-ESIPT weak blue to ESIPT strong green fluorescence. This ESIPT fluorescent chromic behaviour for strong bases such as NH_3 and R-NH_2 was manifested via a two-step process (Fig. 18c), where the fluorescence changed from weak non-ESIPT blue, to strong ESIPT blue, and finally to strong non-ESIPT green emission in solids. The detection limit of the NH_3 molecule was approximately 10 ppm using a spin-coated SHBT thin film. Single-crystal X-ray structural analyses of $(C_3H_7NH_2)(SHBT)$ and $(C_3H_7NH_2)_2(SHBT)$ clarified the molecular structures of each SHBT variant, forming H^+-transferred $(C_3H_7NH_3^+)(SHBT^-)$ and $(C_3H_7NH_3^+)_2(SHBT^{2-})$, respectively. The former monoanionic SHBT$^-$ has an O−H•••N hydrogen-bonding ESIPT conformation with strong green-coloured ESIPT fluorescence, while the latter dianionic species has two different anionic sites (–SO_3^- and −O^-) with the non-ESIPT conformation, which does not possess intramolecular O−H•••N hydrogen-bonding interactions, and shows non-ESIPT blue-coloured fluorescence. These examples of two-step ESIPT fluorescent chromism occurred in a highly crystalline state based on the change in the PXRD patterns, where the rotational dynamics of the benzothiazole unit in the solid enabled the ESIPT conformation to be switched on and off. The conformational freedom and fluorescent chromic behaviour were coupled to each other, which is advantageous for designing multifunctional external-stimuli responsive materials.

7. Summary and feature perspective

This review discusses the roles of H^+, M^+, molecules, and crystal lattices as dynamic structural units in molecular assemblies. These assemblies involve diverse intermolecular interactions, including strong electrostatic, hydrogen-bonding, CT, and weak van der Waals interactions. The motional freedom of small H^+ ions encompasses short- and long-range dynamics in ferroelectrics and H^+ conductors, respectively, while the dynamic M^+ motions of Li^+ and Na^+ involve ionic conductors and the coupling to the conduction electrons as a pinning potential. The softness and hardness of crystal lattices are modulated by replacing M^+ cations, such as Li^+, Na^+, K^+, Rb^+, and Cs^+, with an n-type organic semiconductor in the form of dianionic NDI derivatives. The dynamics of molecular rotation in plastic crystals and liquid crystals are well established, although their role in the design of physical properties have yet to be sufficiently examined. The use of a polar rotator structure based on a supramolecular approach enables the formation of ferroelectric molecular crystals. Hydrogen-bonding molecular crystals are also interesting structural motifs for enabling reversible molecular adsorption–desorption. Further investigation of these host–guest molecular systems resulted in ESIPT fluorescent chromic behaviour and showed interesting molecular sensing properties using various bases, where the dynamic transformation of the crystal lattice and the molecular conformational change were coupled to each other. Recently, such dynamic behaviours have been linked to physical responses including hybrid electrical conduction, ferroelectricity, and fluorescent chromism. In section 2–6, we introduced variety of dynamics form H^+, M^+, molecule, conformation, to crystal lattice. The organic molecular assembly is completely different from the crystal lattice of inorganic compounds, and has a potential to fabricated new multi-functional materials similar to excellent function in biological assembly. A softness of crystal lattice is responsible for various outer stimuli. More complicated dynamic molecular systems such as catenanes and rotaxanes are also interesting structural modules; however, designing motional freedom in solids remains a challenge. Therefore, simple molecular systems are useful as structural units for introducing dynamics into the molecular assembly. In contrast, non-equilibrium dynamic molecular assemblies, such as biological systems, are interesting functional molecular assemblies, where various dynamic processes coexist and couple with each other. However, realising molecular assembly structures that combine the functionalities associated with proteins and low-molecular-weight compounds is an ongoing research objective. One essential point to solve in the near feature is a design of directional motion in molecular assembly. Thermally activated random Brownian motion is never associated with the work of the molecular machine. A possible proposal is an introduction of asymmetry into the motional environment (Brownian ratchet model), which enable to extract the directional motion by the application of external bias. Artificial H^+ pump and molecular motor are the candidate to be designed in molecular assembly. However, exact artificial fabrication of these dynamic

molecular assembly is quite hard task utilising in the present scientific standard. Therefore, the first stage is a coupling of dynamics to physical properties and its understanding in molecular science is the most essential point of view to progress the feature dream for fabricating molecular machines. Achieving protein-like functionality is a goal of our search on artificial molecular motors, and is poised open a new field of molecular science and technology. Nevertheless, coupling dynamic molecular assembly with various physical properties is a useful starting point for realising dynamic hierarchal molecular assembly systems based on functional molecules.

Conflicts of interest

There are no conflicts to declare.

Acknowledgements

Notes and references

1   (a) T. Akutagawa, T. Nakamura, *Dalton Trans*. 2008, 6335–6345; (b) T. Akutagawa, *Mater. Chem. Front*. 2018, **2**, 1064–1073; (c) T. Akutagawa, *Bull. Chem. Soc. Jpn*. 2021 in press.

2   (a) C. Kittel, *Introduction to Solid State Physics*, 8th edition, Wiley, 2005; (b) *Thermal Conductivity*, R. P. Tye ed., Academic Press, 1969; (c) *High Thermal Conductivity Materials*, S. L. Shindé, J. S. Goela eds., Springer, 2005.

3   (a) J. C. Scott, *Semiconductor and Semimetals. High–Conducting Quasi–one–dimensional Organic Crystals*, E. Conwell ed, Academic Press, NY, 1988; (b) T. Ishiguro, K. Yamaji, G. Saito, *Organic Superconductors*, 2nd edition, Springer–Verlag, NY, 1998; (c) D. O. Cowan, *New Aspects of Organic Chemistry*, Z. Yoshida, T. Shiba, Y. Oshiro eds, Kodansha, Tokyo, 1989.

4   (a) B. Albert, D. Bray, A. Johnson, J. Lewis, M. Raff, K. Roberts, P. Walter, *Molecular Biology of the Cell*, Garland Publishing, NY, 1994; (b) L. Stryer, *Biochemistry*, Freeman, NY, 1995.

5   (a) J. K. Whitesell, *Organised Molecular Assemblies in the Solid State,* John Wiley & Sons, NY, 1999; (b) J. Fraxedas, *Molecular Organic Materials. From Molecules to Crystalline Solids*, Cambridge University Pres, 2006; (c) G. Saito, Y. Yoshida, *Bull. Chem. Soc. Jpn*. 2007, **80**, 1–137. (d) J. S. Miller, A. J. Epstein, W. M. Reief, *Science* 1988, **240**, 40–47; (e) J. S. Miller, *Mater. Today* 2014, **17**, 224–235; (f) M. Jiang, Q. Fang, *Adv. Mater*. 1999, **11**, 1147–1151.

6   (a) J. Ferraris, D. O. Cowan, V. Walatka, J. H. Perlstein, *J. Am. Chem. Soc*., 1973, **95**, 948–949; (b) A. J. Heeger, A. F. Garito, *Low–Dimensional Cooperative Phenomena*, H. J. Keller ed., Plenum Press, 1975.

7   (a) N. Fuentes, A. Martín-Lasanta, L. A. de Cienfuegos, M. Ribagorda, A. Parra, J. M. Cuerva, *Nanoscale* 2001, **3**, 4003–4014; (b) F. M. Raymo, R. J. Alvarado, S. Giordani, M. A. Cejas. *J. Am. Chem. Soc*. 2003, **125**, 2361–2364; (c) C. Benesch, M. F. Rode, M. Čížek, R. Härtle, O. Rubio-Pons, M. Thoss, A. Sobolewski, *J. Phys. Chem. C*. 2009, **113**, 10315–10318.

8   (a) P. Chou, D. McMorrow, T. J. Aartsma, M. Kasha, *J. Phys. Chem*. 1984, **88**, 4596–4599; (b) A. U. Acuña, A. Costela, J. M. Muñoz, *J. Phys. Chem*. 1986, **90**, 2807–2808; (c) P. Chou, T. J. Aartsma, *J. Phys. Chem*. 1986, **90**, 721–723; (d) K. Sakai, T. Tsuzuki, Y. Itoh, M. Ichikawa, Y. Taniguchi, *Appl. Phys. Lett*. 2005, **86**, 081103–1–3.

9   (a) J. Heldt, D. Gormin, M. Kasha, *Chem. Phys*. 1989, **136**, 321–334; (b) J. Zhao, S. Ji, Y. Chen, H. Guo, P. Yang, *Phys. Chem. Chem. Phys*. 2012, **14**, 8803–8817; (c) S. Seki, V. S. Padalkar, *Chem. Soc. Rev*. 2016, **45**, 169–202; (d) A. C. Sedgwick, L. Wu, H. -H. Han, S. D. Bull, X. -P. He, T. D. James, J. L. Sessler, B. Z. Tang, H. Tian, J. Yoon, *Chem. Soc. Rev*. 2018, **47**, 8842–8880.

10 (a) S. Horiuchi, Y. Tokura, *Nat. Mater*. 2008, **7**, 357–366; (b) S. Horiuchi, R. Kumai, Y. Tokura, *Angew. Chem. Int. Ed*. 2007, **119**, 3567–3571; (c) S. Horiuchi, Y. Noda, T. Hasegawa, F. Kagawa, S. Ishibashi, *Chem. Mater*. 2015, **27**, 6193–6197; (d) S. Horiuchi, K. Kobayashi, R. Kumai, S. Ishibashi, *Nat. Commun*. 2017, **8**, 14426–1–9.

11 (a) M. F. H. Schuster, W. H. Meyer, M. Schuster, K. D. Kreuer, *Chem. Mater*. 2004, **16**, 329–337; (b) K. Kreuer, S. J. Paddison, E. Spohr, M. Schuster, *Chem. Rev*. 2004, **104**, 4637–4678; (c) J. A. Hurd, R. Vaidhyanathan, V. Thangadurai, C. I. Ratcliffe, I. L. Moudrakovski, G. K. H. Shimizu, *Nat. Chem*. 2009, **1**, 705–710; (d) L. Jiménez–García, A. Kaltbeitzel, V. Enkelmann, J. S. Gutmann, M. Klapper, K. Müllen, *Adv. Func. Mater*. 2011, **21**, 2216–2224.

12 (a) K. Kreuer, A. Rabenau, W. Weppner, *Angew. Chem. Int. Ed*. 1982, **21**, 208–209; (b) N. Agmon, *Chem. Phys. Lett*., 1995, **244**, 456–462; (c) D. Marx, *ChemPhysChem*, 2006, **7**, 1848–1870; (d) G. A. Ludueña, T. D. Kühne, D. Sebastiani, *Chem. Mater*. 2011, **23**, 1424–1429.

13 (a) N. Voyer, M. Robitaille, *J. Am. Chem. Soc*. 1995, **117**, 6599–6600; (b) J. -C. Lassègues, J. Grondin, T. Becker, L. Servant, M. Hernandez, *Solid State Ion.,* 1995, **77**, 311–317; (c) C. Goto, M. Yamamura, A. Satake, Y. Kobuke, *J. Am. Chem. Soc*. 2001, **123**, 12152–12159; (d) S. L. McFarlane, B. A. Day, K. McEleney, M. S. Freund, N. S. Lewis, *Energy Environ. Sci*., 2011, **4**, 1700–1703; (e) T. Muraoka, D. Noguchi, R. S. Kasai, K. Sato, R. Sasaki, K. V. Tabata, T. Ekimoto, M. Ikeguchi, K. Kamagata, N. Hoshino, H. Noji, T. Akutagawa, K. Ichimura, K. Kinbara, *Nat. Commun.*, 2020, **11**, 2494–1–9; (f) S. Zheng, L. Huang, Z. Sun, M. Barboiu, *Angew. Chem. Int. Ed*. 2021, **60**, 566–597.

14 (a) B. Hille, *Ionic Channels of Excitable Membranes*, Sinauer Associates Inc. 1992; (b) *Ionic Channels in Cells and Model System,* R. Latorre, ed., Springer, NY, 1986; (c) B. Eisenberg, *Acc. Chem. Res*. 1998, **31**, 117–123.

15 (a) M. D. Slater, D. Kim, E. Lee, C. S. Johnson, *Adv. Funct. Mater*. 2012, **23**, 947–958; (b) D. Wenwen, L. Xinmiao, W. Xianyong, Q. Jiangfeng, C. Yuliang, A. Xinping, F. Jiwen, Y. Hanxi, *Sci. Rep*. 2013, **3**, 2671–1–6; (c) H. Dong, Y. Liang, O. Tutusaus, R. Mohtadi, Y. Zhang, F. Hao, Y. Yao, *Joule* 2019, **3**, 782–793; (d) B. Park, J. L. Schaefer, *J. Electrochem. Soc*. 2020, **167**, 070545.

16 (a) W. Cochran, *Phys. Rev. Lett*. 1959, **3**, 412–414; (b) W. Cochran, *Adv. Phys*. 1960, **9**, 387–423; M. E. Lens, A. M.

Glass, *Principle and Applications of Ferroelectrics and Related Materials*, Clarendon Press, Oxford, 1977.

17 B. Häupler, A. Wild, U. S. Schubert, *Adv. Energy Mater.* 2015, **5**, 1402034–1–34.

18 (*a*) F. M. Gray, *Polymer Electrolyte*. J. A. Connor ed., RSC, Cambridge, 1997; (*b*) D. E. Fenton, J. M. Parker, P. V. Wright, *Polymer* 1973, **14**, 589–589; (*c*) F. Croce, G. B. Appetecchi, L. Persi, B. Scrosati, *Nature* 1998, **394**, 456–458; (*d*) L. Sieuw, A. Jouhara, E. Quarez, C. Auger, J. F. Gohy, P. Poizot, A. Vlad, *Chem. Sci.* 2019, **10**, 418–426; (*e*) P. Utpalla, S. K. Sharma, K. Sudarshan, S. K. Deshpande, M. Sahu, P. K. Pujari, *J. Phys. Chem. C* 2020, **124**, 4489–4501.

19 (*a*) M. D. Slater, D. Kim, E. Lee, C. S. Johnson, *Adv. Funct. Mater*. 2012, **23**, 947–958; (*b*) D. Wenwen, L. Xinmiao, W. Xianyong, Q. Jiangfeng, C. Yuliang, A. Xinping, F. Jiwen, Y. Hanxi, *Sci. Rep*. 2013, **3**, 2671–1–6; (*c*) H. Dong, Y. Liang, O. Tutusaus, R. Mohtadi, Y. Zhang, F. Hao, Y. Yao, *Joule* 2019, **3**, 782–793; (*d*) B. Park, J. L. Schaefer, *J. Electrochem. Soc.* 2020, **167**, 070545.

20 (*a*) S. -S. Chang, E. R. Jr. Westrum, *J. Phys. Chem*. 1960, **64**, 1547–1551; (*b*) C. E. Nordman, D. L. Schmitkons, *Acta Cryst*. 1965, **18**, 764–767; (*c*) E. Hampton, N. C. Lockhart, J. N. Sherwood, *Chem. Phys. Lett*. 1973, **21**, 191–193; (*d*) R. D. Johnson, C. S. Yannoni, H. C. Dorn, J. R. Salem, D. S. Bethune, *Science* 1992, **255**, 1235–1238; (*e*) R. C. Yu, N. Tea, M. B. Salamon, D. Lorents, R. Malhotra, *Phys. Rev. Lett*. 1992, **68**, 2050–2053; (*f*) N. H. Tea, R. -C. Yu, M. B. Salamon, D. C. Lorents, R. Malhotra, R. S. Ruoff, *Appl. Phys*. 1993, **A56**, 219–225.

21 (*a*) J. N. Sherwood, *The Plastically Crystalline State*, John Wiley & Sons, Chichester, 1979; (*b*) J. Timmermans, *J. Phys. Chem. Solids* 1961, **18**, 1–8; (*c*) H. Suga, S. Seki, *Faraday Discuss. Chem. Soc*. 1980, **69**, 221–240.

22 (*a*) S. D. Woodruff, R. Kopelman, *J. Cryst. Mol. Struct*. 1977, **7**, 29–40; (*b*) T. Atake, H. Gyoten, H. Chihara, *J. Chem. Phys*. 1982, **76**, 5535–5540; (*c*) T. Fujiwara, A. Inaba, T. Atake, *J. Chem. Thermodyn*. 1992, **24**, 863–881; (*d*) M. Frankosky, J. G. Aston, *J. Phys. Chem*. 1965, **69**, 3126–3132; (*e*) E. E. Burnell, C. A. de Lange, W. L. Meerts, *J. Chem. Phys*. 2016, **145**, 091101–1–5.

23 (*a*) *Disorder in Crystals*, N. G. Parsonage, L. A. K. Staveley eds., Oxford Univ. Press, 1978; (*b*) *Dynamics of Molecular Crystals*, J. Lascombe, ed., Elsevier, Amsterdam, 1986; (*c*) H. B. Burgi, *Annu. Rev. Phys. Chem*. 2000, **51**, 275–96.

24 (*a*) G. S. Kottas, L. I. Clarke, D. Horinek, J. Michl, *Chem. Rev*. 2005, **105**, 1281–1376; (*b*) T. V. Khuong, J. E. Nuez, C. E. Godinez, M. A. Garcia-Garibay, *Acc. Chem. Res*. 2006, **39**, 413–422; (*c*) R. D. Horansky, L. I. Clarke, J. C. Price, *Phys. Rev. B*. 2005, **72**, 014302–1–5; (*d*) C. Lemouchi, C. S. Vogelsberg, S. Simonov, L. Zorina, P. Batail, S. Brown, M. Garcia-Garibay, *J. Am. Chem. Soc*. 2011, **133**, 6371–6379; (*e*) C. Lemouchi, C. Mézière, L. Zorina, S. Simonov, A. Rodríguez-Fortea, E. Canadell, P. Wzietek, P. Auban-Senzier, C. Pasquier, T. Giamarchi, A. M. Garcia-Garibay, P. Batail, *J. Am. Chem. Soc*. 2012, **134**, 7880–7891.

25 (*a*) R. Bishop, *CrystEngComm*, 2015, **17**, 7448–7460; (*b*) Y. Li, S. Tang, A. Yusov, J. Rose, A. N. Borrfors, C. T. Hu, M. D. Ward, *Nat. Commun*. 2019, **10**, 4477–1–7; (*c*) I. Hisaki, *J. Incl. Phenom. Macro. Chem*. 2020, **96**, 215–231.

26 (*a*) S. Ghosh, C. M. Reddy, *Angew. Chem. Int. Ed*. 2012, **51**, 10319–10323; (*b*) S. Takamizawa, Y. Miyamoto, *Angew. Chem. Int. Ed*. 2014, **53**, 6970–6973; (*c*) S. Hayashi, A. Asano, N. Kamiya, Y. Yokomori, T. Maeda, T. Koizumi, *Sci. Rep*. 2017, **7**, 9453–1–10; (*d*) S. Dey, S. Das, S. Bhunia, R. Chowdhury, A. Mondal, B. Bhattacharya, R. Devarapalli, N. Yasuda, T. Moriwaki, K. Mandal, G. D. Mukherjee, C. M. Reddy, *Nat. Commun*. 2019, **10**, 3711–1–10; (*e*) S. Hayashi, S. Yamamoto, D. Takeuchi, Y. Ie, K. Takagi, *Angew. Chem. Int. Ed*. 2018, **57**,

17002–17008; (*f*) S. Sakamoto, T. Sasaki, A. Sato–Tomita, S. Takamizawa, *Angew. Chem. Int. Ed*. 2019, **131**, 13860–13864; (*g*) S. Das, A. Mondal, C. M. Reddy, *Chem. Soc. Rev*. 2020, **49**, 8878–8896.

27 (*a*) G. Ungar, N. Masic, *J. Phys. Chem*. 1985, **89**, 1036–1042; (b) D. Cholakova, N. Denkov, *Adv. Colloid Interface Sci*. 2019, **269**, 7–42.

28 (*a*) T. Inabe, Y. Matsunaga, Y. Yoshida, *Bull. Chem. Soc. Jpn*. 1979, **52**, 615–616; (*b*) T. Inabe, Y. Matsunaga, Y. Yoshida, *Bull. Chem. Soc. Jpn*. 1979, **52**, 615–616; (*c*) T. Inabe, Y. Matsunaga, M. Nanba, *Bull. Chem. Soc. Jpn*. 1981, **54**, 2557–2564; (*d*) Y. Yoshida, Y. Shimizu, T. Yajima, G. Maruta, S. Takeda, Y. Nakano, T. Hiramatsu, H. Kageyama, H. Yamochi, G. Saito, *Chem. Eur. J*. 2013, **19**, 12313–12324; (*e*) Y. Yoshida, Y. Kumagai, M. Mizuno, K. Isomura, Y. Nakamura, H. Kishida, G. Saito, *Cryst. Growth Des*. 2015, **15**, 11, 5513–5518.

29 (*a*) P. J. Collings, M. Hird, *Introduction to Liquid Crystals, Chemistry and Physics*, G. W. Gray, J. W. Goodby, A. Fukuda eds., Taylor & Francis, London, 1997; (*b*) S. Chandrasekhar, *Liquid Crystals*, Cambridge Univ. Press, NY. 1992; (*c*) T. Zhong, R. Mandle, I. Saez, S. Cowling, J. Gooby, *Liq. Cryst*. 2018, **45**, 2274–2293.

30 (*a*) R. J. Bushby, O. R. Lozman, *Curr. Opin. Coll. Inter. Sci*. 2002, **7**, 343–354; (*b*) T. Wöhrle, I. Wurzbach, J. Kirres, A. Kostidou, N. Kapernaum, J. Litterscheidt, J. C. Haenle, P. Staffeld, A. Baro, F. Giesselmann, S. Laschat, *Chem. Rev*. 2016, **116**, 1139–1241.

31 (*a*) T. Yuge, I. Hisaki, M. Miyata, N. Tohnai, *CrystEngComm* 2008, **10**, 263–266; (*b*) J. Tian, T. -Y. Zhou, S. -C. Zhang, S. Aloni, M. V. Altoe, S. -H. Xie, H. Wang, D. -W. Zhang, X. Zhao, Y. Liu, X. -T. Li, *Nat. Commun*. 2014, **5**, 5574–1–11; (*c*) W. Yang, A. Greenaway, X. Lin, R. Matsuda, A. J. Blake, C. Wilson, W. Lewis, P. Hubberstey, S. Kitagawa, N. R. Champness, M. Schröder, *J. Am. Chem. Soc*. 2010, **132**, 14457–14469; (*d*) J. Luo, J. -W. Wang, J. -H. Zhang, S. Lai, D. -C. Zhong, *CrystEngComm* 2018, **20**, 5884–5898; (*e*) R. -B. Lin, Y. He, P. Li, H. Wang, W. Zhou, B. Chen, *Chem. Soc. Rev*. 2019, **48**, 1362–1389.

32 (*a*) *Host Guest Complex Chemistry I*, F. Vögtle, ed., Springer 1981; (*b*) *Host–Guest Systems Based on Nanoporous Crystals*, L. Franco, S. Ferdi, S. Ulrich eds., Wiley–VCH, 2003; (*c*) F. H. Herbstein, *Crystalline Molecular Complexes and Compounds Vol. I*, Oxford Science Publications, 2005; (*d*) F. H. Herbstein, *Crystalline Molecular Complexes and Compounds Vol. II*, Oxford Science Publications, 2005.

33 (*a*) A. I. Kitaigorodsky, *Molecular Crystals, and Molecules*, Academic Press, London, 1973; (*b*) A. Gravesite, *Molecular Aggregation: Structure Analysis and Molecular Simulation of Crystals and Liquids*, Oxford Scientific Publication, 2010; (*c*) P. L. Huyskens, W. A. Luck, *Intermolecular Forces. An Introduction to Modern Method and Results*, Zeegers-Huyskens ed., Springer–Verlag, Heidelberg, 1991; (*d*) S. P. Thomas, P. R. Spackman, D. Jayatilaka, M. A. Spackman, *J. Chem. Theory Comput*. 2018, **14**, 1614–162; (*e*) L. J. Prins, D. N. Reinhoudt, P. Timmerman, *Angew. Chem., Int. Ed*. 2001, **40**, 2382–2426; (*f*) M. Stein, M. Heimsaat, *Crystals* 2019, **9**, 665–1–17; (*g*) M. K. Corpino, D. -K. Bučar, *Cryst. Growth Des*. 2019, **19**, 1426–1453.

34 (*a*) G. C. Pimentel, A. L. McClellan, *The Hydrogen Bond*, W. H. Freeman & Co. San Francisco, 1960; (*b*) W. C. Hamilton, J. A. Ibers, *Hydrogen Bonding In Solids*, Benjamin Inc, NY, 1968; (*c*) G. R. Desiraju, T. Steiner, *The Weak Hydrogen Bond*, Oxford Univ. Press, 2001; (*d*) S. Scheiner, *Hydrogen Bonding. A Theoretical Perspective*, Oxford University Press, 1997; (*e*) G. A. Jeffrey, *An Introduction to Hydrogen Bonding*, Oxford University Press, Oxford, 1997; (*f*) T. Steiner, *Angew. Chem., Int. Ed.* 2002, **41**, 49–76.

35 D. Demus, L. Richter, *Textures of Liquid Crystals*, Verlag Chemie, Weinheim, NY, 1978.

36 (*a*) V. F. Lvovivh, *Impedance Spectroscopy*, Wiley, 2012; (*b*) *Solid State Chemistry Techniques*, A. K. Cheetham, P. Day, eds., Oxford Science Publication, 2001; (*c*) *Experimental Techniques in Low-Temperature Physics* 4th ed., G. K. White, P. J. Mession, eds., Oxford Science Publication, 2002.

37 (*a*) M. J. Duer, *Introduction to Solid-state NMR Spectroscopy*, Blackwell Science, 2004; (*b*) S. P. Brown, H. W. Spiess, Steven P. Brown, *Chem. Rev.* 2001, **101**, 4125–4156.

38 (*a*) T. Akutagawa, K. Shitagami, S. Nishihara, S. Takeda, T. Hasegawa, T. Nakamura, Y. Hosokoshi, K. Inoue, S. Ikeuchi, Y. Miyazaki, K. Saito, *J. Am. Chem. Soc.* 2005, **127**, 4397–4402; (*b*) S. Ikeuchi, Y. Miyazaki, S. Takeda, T. Akutagawa, S. Nishihara, T. Nakamura, K. Saito, *J. Chem. Phys.* **2005**, *123*, 044514–1–6.

39 K. C. Kao, *Dielectric Phenomena in Solids*, Elsevier, Amsterdam, 2004.

40 F. Jona, G. Shirane, *Ferroelectric Crystals*, Dover Publications Inc., NY, 1993.

41 (*a*) T. Hang, W. Zhang, H. -Y. Ye, R. -G. Xiong, *Chem. Soc. Rev.*, 2011, **40**, 3577–3598; (*b*) W. Zhang, R. -G. Xiong, *Chem. Rev.* 2012, **112**, 1163–1195; (*c*) A. S. Tayi, A. Kaeser, M. Matsumoto, T. Aida, S. I. Stupp, *Nat. Chem.* 2015, **7**, 281–294; (*d*) A. V. Gorbunov, M. Garcia Iglesias, J. Guilleme, T. D. Cornelissen, W. S. C. Roelofs, T. Torres, D. González–Rodríguez, E. W. Meijer, M. Kemerink, *Sci. Adv.* 2017, **3**, e1701017–1–7; (*e*) P. -F. Li, W. -Q. Liao, Y. -Y. Tang, W. Qiao, D. Zhao, Y. Ai, Y. -F. Yao, R. -G. Xiong, *Proc. Nat. Acad. Sci. U. S. A*, 2019, **26**, 5878–5885; (*f*) H. -Y. Zhang, H. -Y. Zhang, Y. -Y. Tang, P. -P. Shi, R. -G. Xiong, *Acc. Chem. Res.* 2019, **52**, 1928–1938.

42 (*a*) M. Fukunaga, Y. Noda, *J. Phys. Soc. Jpn.* 2008, **77**, 064706–1–5; (*b*) T. Evans, *Characterizing Ferroelectric Materials*, Radiant Technol. Inc., New Mexico, 2011. PUND measurement

43 (*a*) G. E. Murch, *Solid State Ion.*, 1982, **7**, 177–198; (*b*) K. L. Nagi, *Solid State Ion.*, 1981, **5**, 27–33.

44 (*a*) D. Sato, T. Akutagawa, S. Takeda, S. Noro, T. Nakamura, *Inorg. Chem.* 2007, **46**, 363–365; (*b*) T. Akutagawa, D. Sato, H. Koshinaka, M. Aonuma, S. Noro, S. Takeda, T. Nakamura, *Inorg. Chem.* 2008, **47**. 5951–5962.

45 S. Nishihara, T. Akutagawa, D. Sato, S. Takeda, S. Noro, T. Nakamura, *Chem. Asian J.* 2007, **2**, 1083–1090.

46 (*a*) J. P. Guthrie, *Chem. Bio.* 1996, **3**, 163–l70; (*b*) H. Adalsteinsson, A. H. Maulitz, T. C. Bruice, *J. Am. Chem. Soc.* 1996, **118**, 7689–7693; (*c*) *Hydrogen Bonding—New Insights*, S. J. Grabowski, ed., Springer, 2006; (*d*) G. J. Kearley, F. Fillaux, M. -H. Baron, S. Bennington, J. Tomkinson, *Science*, 1994, **264**, 1285–1289.

47 (*a*) N. C. Deno, H. J. Peterson, G. S. Saines, *Chem. Rev.* 1960, **60**, 7–14; (*b*) G. Saito, A. K. Colter, *Tetrahedron Lett.*, 1977, **38**, 3325–3328; (*c*) A. K. Colter, G. Saito, F. J. Sharom, A. P. Hong, *J. Am. Chem. Soc.* 1976, **98**, 7833–7835.

48 (*a*) T. Akutagawa, T. Uchimaru, K. Sakai, T. Hasegawa, T. Nakamura, *J. Phys. Chem. B*. 2003, **107**, 6248–6251; (*b*) P. Gilli, L. Pretto, G. Gilli, *J. Mol. Struct*. 2007, **844–845**, 328–339; (*c*) P. Gilli, L. Pretto, V. Bertolasi, G. Gilli, *Acc. Chem. Res.* 2009, **42**, 33–44.

49 (*a*) G. Gilli, P.Gilli, *J. Mol. Struct*. 2000, **552**, 1–15; (*b*) V. W. Day, M. A. Hossain, S. O. Kang, D. Powell, G. Lushington, K. Bowman-James, *J. Am. Chem. Soc.* 2007, **129**, 8692–8693; (*c*) B. Schiøtt, B. B. Iversen, G. K. H. Madsen, F. K. Larsen, T. C. Bruice, *Proc. Nat. Acad. Sci. U. S. A* 1998, **95**, 12799–12802; (*d*) C. L. Perrin, J. B. Nielson, *Annu. Rev. Phys. Chem*. 1997. **48**, 511–555.

50 (*a*) C. Svensson, S. C. Abrahams, J. L. Bernstein, R. C. Haddon *J. Am. Chem. Soc.* 1979, **101**, 5759–5764; (*b*) R. C. Haddon, *J. Am. Chem. Soc*. 1980, **102**, 1807–1811; (*c*) R. Rossetti, R. C. Haddon, L. E. Brus, *J. Am. Chem. Soc*. 1980, **102**, 6913–6916; (*d*) S. C. Abrahams, H. E. Bair, R. C. Haddon, F. H. Stillinger, C. Svensson, *J. Chem. Phys*. 1981, **74**, 644–646; (*e*) A. Jayaraman, G. A. Kourouklis, R. C. Haddon, *J. Chem. Phys*. 1987, **87**, 3587–3590.

51 (*a*) T. Mochida, A. Izuoka, T. Sugawara, Y. Moritomo, Y. Tokura, *J. Chem. Phys*. 1994, **101**, 7971; (*b*) Y. Moritomo, Y. Tokura, T. Mochida, A. Izuoka, T. Sugawara, *J. Phys. Soc. Jpn*. 1995, **64**, 1892–1895; (*c*) T. Matsuo, K. Kohno, A. Inaba, T. Mochida, A. Izuoka, T. Sugawara, *J. Chem. Phys*. 1998, **108**, 9809–1–9; (*d*) Y. Noda, I. Tamura, Y. Kuroiwa, T. Mochida, T. Sugawara, *J. Phys. Soc. Jpn*. 1994, **63**, 4286–4289; (*e*) R. Kiyanagi, H. Kimura, M. Watanabe, Y. Noda, T. Mochida, T. Sugawara, *J. Phys. Soc. Jpn*. 2008, **77**, 064602–1–7; (f) H. Otaki, K. Ando, *Phys. Chem. Chem. Phys*. 2011, **13**, 10719–10728.

52 (*a*) S. Koval, J. Kohanoff, R. L. Migoni, E. Tosatt, *Phys. Rev. Lett*. 2002, **89**, 187602–1–4; (*b*) G. F. Reiter, J. Mayers, P. Platzman, *Phys. Rev. Lett*. 2002, **89**, 135505–1–4; (*c*) V. H. Schmidt, *Ferroelectrics* 1987, **72**, 157–173.

53 (*a*) S. J. Formosinho, L. G. Arnaut, *J. Photo. Photobio. A*, 1993, **75**, 21–48; (*b*) L. M. Tolbert, K. M. Solntsev, *Acc. Chem. Res*. 2002, **35**, 19–27; (*c*) N. Agmon, *J. Phys. Chem. A* 2005, **109**, 13–35; (*d*) P. Zhou, K. Han, *Acc. Chem. Res*. 2018, **51**, 1681–1690.

54 (*a*) D. P. Murale, H. Kim, W. S. Choi, D. G. Churchill, *Org. Lett*. 2013, **15**, 3946–3949; (*b*) L. Feng, Z. -M. Liu, J. Hou, X. Lv, J. Ning, G. -B. Ge, J. -N. Cui, L. Yang, *Biosens. Bioelect*. 2015, **65**, 9–15; (*c*) A. C. Sedgwick, L. Wu, H. -H. Han, S. D. Bull, X. -P. He, T. D. James, J. L. Sessler, B. Z. Tang, H. Tian, J. Yoon, *Chem. Soc. Rev*. 2018, **47**, 8842–8880.

55 (*a*) G. A. Samara, D. Semmingsen, *J. Chem. Phys*. 1979, **71**, 1401–1407; (*b*) Y. Moritomo, S. Koshihara, Y. Tokura, *J. Chem. Phys*. 1990, **93**, 5429–5435.

56 S. Horiuchi, Y. Tokunaga, G. Giovannetti, S. Picozzi, H. Itoh, R. Shimano, R. Kumai, Y. Tokura, *Nature* 2010, **463**, 789–792.

57 A. Katrusiak, M. Szafrański, *Phys. Rev. Lett*. 1999, **82**, 576–579.

58 T. Akutagawa, S. Takeda, T. Hasegawa, T. Nakamura, *J. Am. Chem. Soc*. 2004, **126**, 291–294.

59 (*a*) H. E. Katz, Z. Bao, *J. Phys. Chem. B* 2000, **104**, 671–678; (*b*) H. Sirringhaus, *Adv. Mater*. 2014, **26**, 1319–1335; (*c*) L. Torsi, M. Magliulo, K. Manoli, G. Palazzo, *Chem. Soc. Rev*. 2013, **42**, 8612–8628; (*d*) A. F. Paterson, S. Singh, K. J. Fallon, T. Hodsden, Y. Han, B. C. Schroeder, H. Bronstein, M. Heeney, I. McCulloch, T. D. Anthopoulos, *Adv. Mater*. 2018, **30**, 1801079–1–33.

60 J. Otomo, N. Minagawa, C. Wen, K. Eguchi, H. Takahashi, *Solid State Ion.* 2003, **156**, 357–369.

61 Y. Yoshii, N. Hoshino, T. Takeda, T. Akutagawa, *J. Phys. Chem. C*. 2015, **119**, 20845–20854

62 G. Yuan, T. Takeda, N. Hoshino, T. Akutagawa, *J. Phys. Chem. C*. 2020, **124**, 186–187.

63 (*a*) G. Saito, Y. Matsunaga, *Bull. Chem. Soc. Jpn*., 1971, **44**, 2214–2215; (*b*) G. Saito, Y. Matsunaga, *Bull. Chem. Soc. Jpn*., 1971, **44**, 3328–3335; (*c*) G. Saito, Y. Matsunaga, *Bull. Chem. Soc. Jpn*., 1973, **46**, 1609–1616.

64 T. Sakurai, *Acta Cryst*. 1965, **19**, 320–330.

65 (*a*) T. Mitani, G. Saito, H. Urayama, *Phys. Rev. Lett*. 1988, **60**, 2299–2302; (*b*) Y. Shigeta, H. Nagao, J. Toyoda, Y. Morita, K. Nakasuji, Y. Yoshioka, K. Yamaguchi, *Int. J. Quant. Chem*. 2000, **80**, 882–891; (*c*) K. Nakasuji, T. Kitagawa, K. Okaniwa, T. Mitani, *J. Am. Chem. Soc*. 1991, **113**, 1862–1864.

66 (*a*) T. Isono, H. Kamo, A. Ueda, K. Takahashi, A. Nakao, R. Kumai, H. Nakao, K. Kobayashi, Y. Murakami, H. Mori, *Nat. Commun*. 2013, **4**, 1344–1–6; (*b*) T. Isono, H. Kamo, A. Ueda, K. Takahashi, M. Kimata, H. Tajima, S. Tsuchiya, T. Terashima,

S. Uji, H. Mori, *Phys. Rev. Lett*. 2014, **112**, 177201–1–5; (*c*) A. Ueda, K. Kishimoto, Y. Sunairi, J. Yoshida, H. Yamakawa, T. Miyamoto, T. Terashige, H. Okamoto, H. Mori, *J. Phys. Soc. Jpn*. 2019, **88**, 034710–1–6.

67 (*a*) T. Akutagawa, G. Saito, *Bull. Chem. Soc. Jpn*. 1995, **68**, 1753–1773; (*b*) T. Akutagawa, G. Saito, M. Kusunoki, K. Sakaguchi, *Bull. Chem. Soc. Jpn*. 1996, **69**, 2487–2511.

68 (*a*) T. Akutagawa, G. Saito, H. Yamochi, M. Kusunoki, K. Sakaguchi, *Synth. Met*. 1995, **69**, 591–592; (*b*) T. Akutagawa, G. Saito, T. Nakamura, K. Sakaguchi, M. Kusunoki, *Mol. Cryst. Liq. Cryst*. 1996, **276**, 257–266; (*c*) T. Akutagawa, T. Hasegawa, T. Nakamura, G. Saito, *CrystEngComm* 2003, **5,** 54–57; (*d*) T. Akutagawa, T. Hasegawa, T. Nakamura, T. Inabe, G. Saito, *Chem. Eur. J*. **2002**, *8*, 4402–4411.

69 (*a*) H. Kitagawa, H. Okamoto, T. Mitani, M. Yamashita, *Mol. Cryst. Liq. Cryst*. 1993, **228**, 155–160; (*b*) K. -i. Sakai, H. Kitagawa, T. Mitani, M. Yamashita, *Chem. Lett*., 1997, **1997**, 1237–1238; (*c*) K. Saito, Y. Yamamura, H. Kitagawa, D. Yoshida, T. Mitani, M. Sorai, *J. Phys. Soc. Jpn*. 1999, **68**, 3592–3599.

70 (*a*) Y. Inaguma, M. Itoh, *Solid State Ionics*, 1996, **86–88**, 257–260; (*b*) T. Ishigaki, S. Yamauchi, K. Kishio, J. Mizusaki, K. Fueki, *J. Solid State Chem*., 1988, **73**, 179–187.

71 (*a*) K. S. Åkerfeldt, J. D. Lear, Z. R. Wasserman, L. A. Chung, W. F. DeGrado, *Acc. Chem. Res*. 1993, **26**, 191–197; (*b*) M. R. Ghadiri, J. R. Granja, L. K. Buehler, *Nature*. 1994, **369**, 301–304; (*c*) G. W. Gokel, O. Murillo, *Acc. Chem. Res*. 1996, **29,** 425–432; (*d*) J. -C. Meillon, N. Voyer, *Angew. Chem. Int. Ed.* 1997, **36**, 967–969; (*e*) O. Murillo, I. Suzuki, E. Abel, C. L. Murray, E. S. Meadows, T. Jin, G. W. Gokel, *J. Am. Chem. Soc*. 1997, **119**, 5540–5549; (*f*) G. W. Gokel, *Chem. Commun*. 2000, **2000**, 1–9.

72 (*a*) R. M. Izatt, J. S. Bradshaw, S. A. Nielsen, J. D. Lamb, J. J. Christensen, D. Sen, *Chem. Rev*. 1985, **85**, 271; (*b*) R. M. Izatt, K. Pawlak, J. D. Bradshaw, R. L. Bruening, *Chem. Rev*. 1991, **91**, 1721–2085; (*c*) E. Weber, J. L. Toner, I. Goldberg, F. Vögtle, D. A. Laidler, J. F. Stoddart, R. A. Bartsch, C. L. Liotta, *Crown ethers and analogs*, S. Patai, Z. Rappoport eds., John Wiley & Sons, NY, 1989; (*d*) G. W. Gokel, *Crown Ethers & Cryptands*, J. F. Stoddart ed., RSC, Cambridge, 1994.

73 (*a*) T. Akutagawa, T. Nakamura, *Coord. Chem. Rev*. 2002, **226**, 3–9; (*b*) S. Nishihara, T. Akutagawa, T. Hasegawa, S. Fujiyama, T. Nakamura, T. Nakamura, *J. Solid State Chem*. 2002, **168**, 661–667; (c) S. Nishihara, T. Akutagawa, T. Hasegawa, T. Nakamura, *Chem. Commun*. 2002, 408–409; (*d*) T. Akutagawa, A. Hashimoto, S. Nishihara, T. Hasegawa, T. Nakamura, *J. Phys. Chem. B* 2003, **107**, 66–74; (*e*) T. Akutagawa, K. Matsuura, A. Hashimoto, T. Nakamura, *Inorg. Chem*. 2005, **44**, 4454–4456; (*f*) T. Akutagawa, D. Sato, Q. Ye, S. -i. Noro, T. Nakamura, *Dalton Trans*. 2010, **39**, 2191–2193; (*g*) T. Akutagawa, H. Koshinaka, Q. Ye, S. -I. Noro, J. Kawamata, H. Yamaki, T. Nakamura, *Chem. Asian J*. 2010, **5**, 520–529; (*h*) T. Akutagawa, D. Sato, Q. Ye, T. Endo, S. -I. Noro, S. Takeda, T. Nakamura, *Dalton Trans*. 2010, **39**, 8219–8227.

74 (*a*) K. Sambe, N. Hoshino, T. Takeda, T. Nakamura, T. Akutagawa, *Cryst. Growth Des*. 2020, **20**, 3625–3634; (*b*) K. Sambe, N. Hoshino, T. Takeda, T. Nakamura, T. Akutagawa, *J. Phys. Chem. C*. 2020, **124**, 13560–13571.

75 C. Kato, R. Machida, R. Maruyama, R. Tsunashima, X. -M. Ren, M. Kurmoo, K. Inoue, S. Nishihara, *Angew. Chem. Int. Ed*. 2018, **57**, 13429–13432.

76 (*a*) T. Nakamura, T. Akutagawa, K. Honda, A. E. Underhill, A. T. Coomber, R. H. Friend, *Nature* 1998, **394**, 159–160; (*b*) T. Akutagawa, T. Hasegawa, T. Nakamura, S. Takeda, T. Inabe, K. Sugiura, Y. Sakata, A. E. Underhill, *Chem. Eur. J*. 2001, **7**, 4902–4912; (*c*) T. Akutagawa, S. Takeda, T. Hasegawa, T. Nakamura, *J. Am. Chem. Soc*. 2004, **126**, 291–294.

77 (*a*) T. Matsumoto, T. Nogami, H. Tanaka, H. Mikawa, Synthesis, *Bull. Chem. Soc. Jpn*. 1982, **55**, 369–373; (*b*) K. Matsuoka, T. Nogami, T. Matsumoto, H. Tanaka, H. Mikawa H. *Bull. Chem. Soc. Jpn*. 1982, **55**, 2015–2020; (*c*) T. Nogami, M. Morinaga, H. Mikawa, H. Nakano, M. Horioka, H. Horiuchi, M. Tokonami, *Bull. Chem. Soc. Jpn*. 1990, **63**, 2414–2416; (*d*) B. Yan, P. N. Horton, A. E. Russell, C. J. Wedge, S. C. Weston, M. C. Grossel, *CrystEngComm*, 2019, **21**, 3273–3279.

78 (*a*) A. Kawasaki, T. Takeda, N. Hoshino, W. Matsuda, S. Seki, T. Akutagawa, *J. Phys. Chem. C*. 2019, **123**, 15451–15457; (*b*) A. Kawasaki, T. Takeda, N. Hoshino, W. Matsuda, S. Seki, T. Akutagawa, *Cryst. Growth Des*. 2020, **20**, 1276–1284.

79 (*a*) H. Abe, A. Kawasaki, T. Takeda, N. Hoshino, W. Matsuda, S. Seki, T. Akutagawa, *ACS Appl. Mater. Inter.* 2020, **12**, 37391–37399; (*b*) H. Abe, A. Kawasaki, T. Takeda, N. Hoshino, W. Matsuda, S. Seki, T. Akutagawa, *J. Am. Chem. Soc*. 2021, **143**, 1046–1060.

80 (*a*) J. C. Hummelen, G. Yu, J. Gao, F. Wudl, A. J. Heeger, *Science* 1995, **270**, 1789–1791; (*b*) T. Ameri, P. Khoram, J. Min, C. J. Brabec, *Adv. Mater*. 2013, **25**, 4245–4266.

81 (*a*) J. Harada, T. Shimojo, H. Oyamaguchi, H. Hasegawa, Y. Takahashi, K. Satomi, Y. Suzuki, J. Kawamata, T. Inabe, *Nat. Chem*. 2016, **8**, 946–952; (*b*) J. Harada, Y. Kawamura, Y. Takahashi, Y. Uemura, T. Hasegawa, H. Taniguchi, K. Maruyama, *J. Am. Chem. Soc*. 2019, **141**, 9349–9357.

82 (*a*) Y. Zhang, X. -J. Song, Z. -X. Zhang, D. -W. Fu, R. G. Xiong, *Matter* 2020, **2**, 697–710; (*b*) H. -Y. Ye, J. -Z. Ge, Y. -Y. Tang, P. -F. Li, Y. Zhang, Y. -M. You, R. -G. Xiong, *J. Am. Chem. Soc*. 2016, **138**, 13175–13178; (*c*) Y. Xie, Y. Ai, Y. -L. Zeng, W. -H. He, X. -Q. Huang, D. -W. Fu, J. -X. Gao, X. -G. Chen, Y. -Y. Tang, *J. Am. Chem. Soc*. 2020, **142**, 12486–12492.

83 (*a*) N. Hoshino, T. Takeda, T. Akutagawa, *RSC Adv.* 2013, **4**, 743–747; (*b*) S. Matsumoto, T. Higashiyama, H. Akutsu, S. Nakatsuji, *Angew. Chem. Int. Ed*. 2011, **50**, 10879–10883.

84 J. Ichikawa, N. Hoshino, T. Takeda, T. Akutagawa, *J. Am. Chem. Soc*. 2015, **137**, 13155–13160.

85 (*a*) T. C. Bedard, J. S. Moore, *J. Am. Chem. Soc*. 1995, **117**, 10662–10671; (*b*) N. Zigon, P. Larpent, A. Jouaiti, N. Kyritsakasa, M. W. Hosseini, *Dalton Trans*., 2014, **43**, 15779–15784; (*c*) T. Lang, A. Guenet, E. Graf, N. Kyritsakas, M. W. Hosseini, *Chem. Commun*. 2010, **46**, 3508–3510.

86 (*a*) M. A. Garcia-Garibay, *Proc. Natl. Acad. Sci. U. S. A*. 2005, **102**, 10771–10776; (*b*) C. S. Vogelsberg, M. A. Garcia-Garibay, *Chem. Soc. Rev*. 2012, **41**, 1892–1910; (*c*) Z. Dominguez, H. Dang, M. J. Strouse, M. A. Garcia-Garibay, *J. Am. Chem. Soc*. 2002, **124**, 7719–7727; (*d*) Z. Dominguez, H. Dang, M. J. Strouse, M. A. Garcia-Garibay, *J. Am. Chem. Soc*. 2002, **124**, 2398–2399; (*e*) S. L. Gould, D. Tranchemontagne, O. M. Yaghi, M. A. Garcia-Garibay, *J. Am. Chem. Soc*. 2008, **130**, 3246–3247; (*f*) P. Commins, M. A. Garcia-Garibay, *J. Org. Chem*. 2014, **79**, 1611–1619.

87 (*a*) T. Akutagawa, D. Sato, H. Koshinaka, M. Aonuma, S. Noro, S. Takeda, T. Nakamura, *Inorg. Chem*. 2008, **47**, 5951–5962; (*b*) T. Akutagawa, D. Sato, Q. Ye, S. -i. Noro, T. Nakamura, *Dalton Trans*. 2010, **39**, 2191–2193; (*c*) T. Akutagawa, H. Koshinaka, Q. Ye, S. -I. Noro, J. Kawamata, H. Yamaki, T. Nakamura, *Chem. Asian J*. 2010, **5**, 520–529.

88 T. Akutagawa, H. Koshinaka, D. Sato, S. Takeda, S. –i. Noro, H. Takahasi, R. Kumai, Y. Tokura, T. Nakamura, T. *Nat. Mater*. 2009, **8**, 342–347.

89 (*a*) S. T. Lagerwall, I. Dahl, *Mol. Cryst. Liq. Cryst*. 1984, **114**, 151–187; (*b*) S. T. Lagerwall, *Ferroelectrics* 2004, **301**, 15–45; (*c*) R. B. Meyer, *Mol. Cryst. Liq. Cryst*. 1977, **40**, 133–48.

90 Y. Matsunaga, N. Miyajima, Y. Nakayasu, S. Sakai, M. Yonenaga, *Bull. Chem. Soc. Jpn*. 1988, **61**, 207–210.

91 (*a*) Y. Yasuda, E. Iishi, H. Inada, Y. Shirota, *Chem. Lett*. 1996, **25**, 575–576; (*b*) K. Hanabusa, C. Koto, M. Kimura, H. Shirai, A. Kakehi, *Chem. Lett*. 1997, 429–430.

92 (*a*) C. F. C. Fitié, W. S. C. D. Roelofs, M. Kemerink, R. P. Sijbesma, *J. Am. Chem. Soc*. 2010, **132**, 6892–6893; (*b*) C. F. C. Fitié, W. S. C. Roelofs, P. C. M. M. Magusin, M. Wübbenhorst, M. Kemerink, R. P. Sijbesma, *J. Phys. Chem. B* 2012, **116**, 3928–3937; (*c*) I. Urbanaviciute, X. Meng, T. D. Cornelissen, A. V. Gorbunov, S. Bhattacharjee, R. P. Sijbesma, M. Kemerink, *Adv. Electron. Mater*. 2017, **3**, 1600530–1–7; (*d*) I. Urbanaviciute, S. Bhattacharjee, M. Biler, J. A. M. Lugger, T. D. Cornelissen, P. Norman, M. Linares, R. P. Sijbesma, M. Kemerink, *Phys. Chem. Chem. Phys*. 2019, **21**, 2069–2079; (*e*) J. Wu, T. Takeda, N. Hoshino, T. Akutagawa, *J. Mater. Chem. C*. 2020, **8**, 10283–10289.

93 Y. Shishido, H. Anetai, T. Takeda, N. Hoshino, S. Noro, T. Nakamura, T. Akutagawa, *J. Phys. Chem. C*. 2014, **118**, 21204–21214.

94 (*a*) T. Förster, *Angew. Chem., Int. Ed. Eng*. 1969, **8**, 333–343; (*b*) T. M. Figueira-Duarte, K. Müllen, *Chem. Rev*. 2011, **111**, 7260–7314; (*c*) J. M. Casas-Solvas, J. D. Howgego, A. P. Davis, *Org. Biomol. Chem*. 2014, **12**, 212–232.

95 H. Anetai, Y. Wada, T. Takeda, N. Hoshino, S. Yamamoto, M. Mitsuishi, T. Takenobu, T. Akutagawa, *J. Phys. Chem. Lett*. 2015, **6**, 1813–1818.

96 H. Anetai, T. Takeda, N. Hoshino, Y. Araki, T. Wada, S. Yamamoto, M. Mitsuishi, H. Tsuchida, T. Ogoshi, T. Akutagawa, *J. Phys. Chem. C*. 2018, **122**, 6323–6331.

97 H. Anetai, K. Sambe, T. Takeda, N. Hoshino, T. Akutagawa, *Chem. Eur. J*. 2019, **25**, 11233–11239.

98 J. Wu, T. Takeda, N. Hoshino, T. Akutagawa, *J. Phys. Chem. B*., 2020, **124**, 7067–7074.

99 H. Anetai, T. Takeda, N. Hoshino, H. Kobayashi, N. Saito, M. Shigeno, M. Yamaguchi, T. Akutagawa, *J. Am. Chem. Soc*. 2019, **141**, 2391–2397.

100 (*a*) H. Sakurai, T. Daiko, T. Hirao, *Science* 2003, **301**, 1878–1878; (*b*) D. Halilovic, M. Budanovic, Z. R. Wong, R. D. Webster, J. Huh, M. C. Stuparu, *J. Org. Chem*. 2018, **83**, 3529–3536.

101 (*a*) W. E. Barth, R. G. Lawton, *J. Am. Chem. Soc*. 1966, **88**, 380–381; (*b*) L. T. Scott, M. M. Hashemi, D. T. Meyer, H. B. Warren, *J. Am. Chem. Soc*. 1991, **113**, 7082–7084; (*c*) T. J. Seiders, K. K. Baldridge, G. H. Grube, J. S. Siegel, *J. Am. Chem. Soc*. 2001, **123**, 517–525.

102 K. Imamura, K. Takimiya, T. Otsubo, Y. Aso, *Chem. Commun*. 1999, 1859–860.

103 S. Furukawa, J. Wu, M. Koyama, K. Hayashi, N. Hoshino, M. Saito, T. Akutagawa, *Nat. Commun.* 2021, **12,** 768–1–9.

104 (*a*) R. Kind, *Ferroelectrics*, 1980, **24**, 81–88; (*b*) I. R. Jahn, K. Schwab, K. Knorr, K. Holocher, *J. Phys. Condens. Matter* 1994, **6**, 10839–10853.

105 (*a*) L. J. De Jongh, A. C. Botterman, F. R. De Boer, A. R. Miedema, *J. Appl. Phys*. 1969, **40**, 1363–1365; (*b*) L. J. De Jongh, W. D. van Amstel, A. R. Miedema, *Physica*, 1972, **58**, 277.

106 (*a*) B. Kundys, A. Lappas, M. Viret, V. Kapustianyk, V. Rudyk, S. Semak, C. Simon, I. Bakaimi, *Phys. Rev. B* 2010, **81**, 224434–1–6; (*b*) B. Huang, J. -Y. Zhang, R. -K. Huang, M. -K. Chen, W. Xue, W. -X. Zhang, M. -H. Zeng, X. -M. Chen, *Chem. Sci*. 2018, **9**, 7413–7418.

107 N. Hoshino, S. Tamura, T. Akutagawa, *Chem. Eur. J*. 2020, **26**, 2610–2618.

108 S. van Smaalen, *Incommensurate Crystallography*, Oxford University Press, Oxford, 2007.

109 *Thermal conductivity: theory, properties, and applications*, T. Tritt ed., Kruwer, Academic Plenum Publishers, NY, 2004.

110 N. Hoshino, T. Akutagawa, *Chem. Phys. Lett*. 2020, **153**, 194503–1–8.

111 M. Mastalerz, I. M. Oppel, *Angew. Chem. Int. Ed*. 2012, **51**, 5252–5255.

112 (*a*) *Supramolecular Assembly via Hydrogen Bonds I*, D.M. P. Mingos ed., Springer, 2004; (*b*) *Supramolecular Assembly via Hydrogen Bonds II*, D.M. P. Mingos ed., Springer, 2004.

113 (*a*) J. Yang, M. B. Dewal, L. S. Shimizu, *J. Am. Chem. Soc*. 2006, **128**, 8122–8123; (*b*) M. B. Dewal, M. W. Lufaso, A. D. Hughes, S. A. Samuel, P. Pellechia, L. S. Shimizu, *Chem. Mater*. 2006, **18**, 4855–4864; (*c*) M. B. Dewal, Y. Xu, J. Yang, F. Mohammed, M. D. Smith, L. S. Shimizu, *Chem. Commun*. 2008, **33**, 3909–3911.

114 G. Yuan, T. Takeda, N. Hoshino, T. Akutagawa, *Cryst. Growth De*s. 2019, **19**, 3509–3517.

115 H. Nishiyama, N. Hoshino, T. Takeda, K. Takahashi, S. -i. Noro, T. Nakamura, T. Akutagawa, *Cryst. Growth Des*. 2018, **18**, 286–296.

116 (*a*) V. A. Russell, M. C. Etter, M. D. Ward, *Chem. Mater*. 1994, **6**, 1206–1217; (*b*) K. T. Holman, A. M. Pivovar, J. A. Swift, M. D. Ward, *Acc. Chem. Res*. 2001, **34**, 107–108; (*c*) K. T. Holman, A. M. Pivovar, M. D. Ward, *Science* 2001, **294**, 1907–1911; (*d*) W. Xiao, C. Hu, M. D. Ward, *J. Am. Chem. Soc*. 2014, **136**, 14200–14206; (*e*) D. J. Plaut, K. T. Holman, A. M. Pivovar, M. D. Ward, *J. Phys. Org. Chem*. 2000, **13,** 858–869; (*f*) K. T. Holman, S. M. Martin, D. P. Parker, M. D. Ward, *J. Am. Chem. Soc*. 2001, **123**, 4421–4431; (*g*) K. T. Holman, M. D. Ward, *Angew. Chem. Int. Ed*. 2000, **39**, 1653–1655; (*h*) I. Brekalo, D. E. Deliz, L. J. Barbour, M. D. Ward, T. Friščić, K. T. Holman. *Angew. Chem. Int. Ed*. 2020, **59**, 1997–2002.

117 H. Abe, T. Kobayashi, N. Hoshino, T. Takeda, Y. Suzuki, J. Kawamata, T. Akutagawa, *CrystEngComm*, 2021, **23**, 1149–1157.

118 (*a*) R.-B. Lin, Y. He, P. Li, H. Wang, W. Zhou, B. Chen, *Chem. Soc. Rev*. 2019, **48**, 1362–1389; (*b*) P. Li, M. R. Ryder, J. F. Stoddart, *Acc. Mater. Res.* 2020, **1**, 77–87; (*c*) M. A. Little, A. I. Cooper, *Adv. Funct. Mater.* 2020, **30**, 1909842; (*d*) I. Hisaki, X. Chen, K. Takahashi, T. Nakamura, *Angew. Chem. Int. Ed.* 2019, **58**, 11160–11170.

119 (*a*) S. Kobatake, S. Takami, H. Muto, T. Ishikawa, M. Irie, *Nature* 2007, **446**, 778–781; (*b*) F. Terao, M. Morimoto, M. Irie, *Angew. Chem. Int. Ed*. 2012, **51**, 901–904; (*c*) H. Koshima, N. Ojima, H. Uchimoto, *J. Am. Chem. Soc.* 2009, **131**, 6890–6891; (*d*) L. Zhu, R. O. Al-Kaysi, R. J. Dillon, F. S. Tham, C. J. Bardeen, *Cryst. Growth Des.* 2011, **11**, 4975–4983; (*e*) P. Naumov, S. C. Sahoo, B. A. Zakharov, E. V. Boldyreva, *Angew. Chem. Int. Ed.* 2013, **52**, 9990–9995.

120 (*a*) N. K. Nath, M. K. Panda, S. C. Sahoo, P. Naumov, *CrystEngComm* 2014, **16**, 1850–1858; (*b*) P. Naumov, S. Chizhik, M. K. Panda, N. K. Nath, E. Boldyreva, *Chem. Rev.* 2015, **115**, 12440–12490; (*c*) P. Commins, I. T. Desta, D. P. Karothu, M. K. Panda, P. Naumov, *Chem. Commun.* 2016, **52**, 13941–13954; (*d*) P. Naumov, D. P. Karothu, E. Ahmed, L. Catalano, P. Commins, J. M. Halabi, M. B. Al-Handawi, L. Li, *J. Am. Chem. Soc.* 2020, **142**, 13256–13272.

121 (*a*) T. Takeda, M. Ozawa, T. Akutagawa, *Cryst. Growth Des.* 2019, **19**, 4784–4792; (*b*) T. Takeda, T. Akutagawa, *Chem. Eur. J.* 2016, **22**, 7763–7770; (*c*) T. Takeda, H. Sugihara, Y. Suzuki, J. Kawamata, T. Akutagawa, *J. Org. Chem.* 2014, **79**, 9669–9676; (*d*) T. Takeda, S. Yamamoto, M. Mitsuishi, T. Akutagawa, *J. Phys. Chem. C* 2018, **122**, 9593–9598; (*e*) T. Takeda, M. Ozawa, T. Akutagawa, *J. Phys. Chem. C* 2019, **123**, 20152–20159; (*f*) T. Takeda, S. Noro, T. Nakamura, Y. Suzuki, J. Kawamata, T. Akutagawa, *CrystEngComm* 2018, **20**, 17–24; (*g*) T. Takeda, T. Akutagawa, *Chem. Commun.* 2020, **56**, 10564–10567.

122 T. Takeda, M. Ozawa, T. Akutagawa, *Angew. Chem. Int. Ed.* 2019*,* **58**, 10345–10352.

Please do not adjust margins

ChemComm

Journal Name

ARTICLE

123   Y. Nakane, T. Takeda, N. Hoshino, K. -i. Sakai, T. Akutagawa, *J. Phys. Chem. C.* 2018, **122**, 16249–16255.

Please do not adjust margins